Flexure of Venusian lithosphere measured from residual topography and gravity

David N. Barnett, Francis Nimmo, and Dan McKenzie
Bullard Laboratories, Department of Earth Sciences, University of Cambridge, Cambridge, England, United Kingdom

Received 19 September 2000; revised 3 August 2001; accepted 20 September 2001; published 26 February 2002.

[1] The elastic lithosphere thickness T_e for various locations on Venus is estimated by modeling lithospheric flexure associated with rifts, coronae, chasmata, and the moats visible around certain large volcanoes. By modeling flexure using the residual topography, a range of elastic thicknesses was found, from around 10 to 40 km or greater. A number of these values are not well-determined and only constrain T_e to be >10 km. The shear stresses predicted from the topography, given these values for T_e, reach several hundred MPa, with surface faulting visible in the synthetic aperture radar (SAR) images at many locations. The elastic thickness was also estimated at seven volcano-like structures by modeling the gravity predicted from the observed topography. This yielded elastic thickness estimates varying between approximately 20 and 60 km, which were generally more tightly constrained. However, an elastic thickness of 25 km fits almost all the observed profiles within uncertainty, and the results from modeling the gravity yield an average global elastic thickness of 29 ± 6 km. There is no evidence that the elastic thickness falls anywhere outside this range. The lack of large-scale regional variations in T_e on Venus, in contrast to the situation observed on the Earth, is consistent with a lack of water and plate tectonics on Venus. *INDEX TERMS:* 6295 Planetology: Solar System Objects: Venus; 8149 Tectonophysics: Planetary tectonics (5475); 1236 Geodesy and Gravity: Rheology of the lithosphere and mantle (8160); 1227 Geodesy and Gravity: Planetary geodesy and gravity (5420, 5714, 6019); *KEYWORDS:* Venus, elastic thickness, lithosphere, flexure, residual topography, gravity

1. Introduction

[2] The elastic thickness T_e is the effective thickness of that part of the lithosphere which can support elastic stresses over geological timescales. T_e is therefore an important geophysical parameter, related to the thermal structure of the interior of the planet. On Earth the elastic thickness exhibits marked regional variations. In the oceans, T_e increases with age, varying between ~5 km or less for spreading ridges and ~30 km for old ocean floor [e.g., *Watts et al.*, 1980]. The base of the elastic layer approximately corresponds to the depth of the 450°C isotherm [*Watts*, 1994]. In continents, there are clear regional variations in T_e, up to values of ~40 km [*McKenzie and Fairhead*, 1997; *Tiwari and Mishra*, 1999; *Maggi et al.*, 2000]. The interiors of fold mountain belts tend to exhibit T_e between about 5 and 10 km, while foreland basins bounding large mountain ranges have elastic thicknesses in the range 15–35 km [see, e.g., *Maggi et al.*, 2000]. The main control on T_e in the continents is likely to be the thermal structure, although the water contents of the lower crust and upper mantle are likely to be involved [*Maggi et al.*, 2000]. It is therefore of interest to investigate whether similar regional variations in T_e are present on Venus, to study the rheological behavior of the Venusian lithosphere.

[3] Flexure of the lithosphere on Venus is observed in two main types of tectonic setting. Uplift occurs on the flanks of large rifts (e.g., in the vicinity of Beta and Atla Regiones, which are generally believed to be the surface expression of active mantle plumes), while downward flexure due to loading of the lithosphere occurs at coronae and chasmata. Modeling of flexure in the space domain is the basis of a class of methods which has been used for determining the elastic thickness of the lithosphere of Venus.

[4] The flexure of the lithosphere may be modeled by assuming a value for the effective elastic thickness. By minimizing the misfit between the theoretical topographic or gravity profiles with those which are observed, as a function of the elastic thickness, T_e at each location may be estimated. *Sandwell and Schubert* [1992] and *Johnson and Sandwell* [1994] modeled the (raw) topography associated with coronae, finding elastic thicknesses in the ranges 15–40 km and 12–34 km, respectively. *Kiefer and Potter* [2000] estimated the elastic thickness by predicting the gravity associated with the observed topography at various shield volcanoes and minimizing the misfit to the observed spherical harmonic gravity. They found values in the range 8–22 km. In addition, *Brown and Grimm* [1996a] modeled elastic flexure for southern Artemis Chasma, yielding a best fit elastic thickness of 56 km, with an uncertainty of at least 10 km, while *Solomon and Head* [1990] modeled flexure at the Freyja Montes foredeep, north of Ishtar Terra, obtaining an elastic thickness between 11 and 18 km. *Brown and Grimm* [1996b] also estimated the elastic thickness of Venus using a flexural model of elastic rebound in large impact craters. They constrained this parameter to be at least 10–15 km in the case of the three largest craters studied. *McGovern and Solomon* [1998] found that the largest 25% of volcanoes on Venus require a T_e of at least 32 km for their growth and support. *Rogers and Zuber* [1998] studied the distribution of concentric graben around the volcanic construct, Nyx Mons, in Bell Regio. They found that an elastic plate thickness of 50 km at the time of load emplacement predicted a stress field in best agreement with the observed distribution of fractures.

[5] The other important class of methods used to calculate elastic thickness is spectral (frequency domain) analysis of gravity and topography. *Barnett et al.* [2000] and *McKenzie and Nimmo* [1997] constrained the elastic thickness for various regions of Venus by calculating the admittance between topography and gravity, using grids of observed line-of-sight (LOS) acceleration

0148-0227/02/2000JE001398$09.00

Table 1. Parameter Values Used in This Study

Parameter	Definition	Value
G	gravitational constant	6.672×10^{-11} m^3 kg^{-1} s^{-2}
a	planetary radius	6052 km
g	acceleration due to gravity	8.86 m s^{-2}
$\Delta\rho$	density contrast between the mantle and the fluid overlying the plate ($\rho_m - \rho_w$)	3300 kg m^{-3}
ρ_m	density of the upper mantle	3300 kg m^{-3}
ρ_c	crustal density	2900 kg m^{-3}
ρ_w	density of overlying fluid	0 kg m^{-3}
t_c	mean crustal thickness	16 km
E	Young's modulus	1×10^{11} Pa
σ	Poisson's ratio	0.25

of the Magellan spacecraft and LOS accelerations calculated from the topography [see *McKenzie*, 1994]. These studies yielded values in the approximate ranges 20–30 km and 10–30 km, respectively. *Smrekar* [1994] and *Phillips* [1994] have calculated the admittance directly from spherical harmonic models of the gravity and topography, giving elastic thickness estimates for Atla of 30 ± 5 km and 25 km [*Phillips et al.*, 1997], respectively. *Smrekar and Stofan* [1999] estimated the elastic thickness at three corona-dominated rises on Venus, using grids of the spherical harmonic gravity and topography and top- and bottom-loading flexural models, the latter of which can take the component of plume support for these regions into account. They found values of 10–20 km for Eastern Eistla, 12–25 km for Central Eistla, and 22–35 km for Themis Regio, depending on whether the top- or bottom-loading models were used. In addition, *Smrekar et al.* [1997] similarly obtained an elastic thickness estimate of 15–40 km for Bell Regio. *Simons et al.* [1997] developed a method for localizing the spherical harmonic gravity and topography fields using axisymmetric windows to calculate the admittance. The spectra obtained implied elastic thicknesses in the range 10–30 km.

[6] For various reasons it is difficult to use previous estimates of T_e for Venus to discover whether there are significant regional variations in this parameter; different authors used different methods to estimate T_e and assumed different crustal thicknesses and values for the elastic moduli. We therefore decided to reexamine the observations using the same approach throughout, in both the frequency domain [*Barnett et al.*, 2000] and the space domain, so that all estimates could be directly compared. To this end, we used the most up-to-date data sets, so that the estimates obtained are the best which are available using our methods. The MGNP180U gravity model itself is a substantial improvement on earlier models [*Konopliv et al.*, 1999] and was used to recalculate the position of Magellan to determine the $l = m = 360$ topography data set [*Rappaport et al.*, 1999].

2. Flexure Measured From Residual Topography

2.1. Introduction and Method

[7] The surface topography of Venus was mapped by the Magellan spaceprobe by picking the first return from a radar signal transmitted downward to the surface at each altimetry point. Recently, the locations of the altimetry points and the associated values for the planetary radius have been recalculated, taking corrections to the position of the spacecraft, derived from the high-resolution gravity model MGNP180U, into account [*Rappaport et al.*, 1999; P. Ford, personal communication, 1999]. This work uses the (gridded) recalculated altimetry points themselves, rather than the spherical harmonic model which was derived from them, as the former has a greater spatial resolution.

[8] Before modeling the lithospheric flexure, it is desirable to remove the long-wavelength component of the topography which is dynamically supported by active convection in the mantle. This removal is achieved by converting the raw topography to residual topography, h_r, defined by

$$h_r = h - \frac{g}{50}, \tag{1}$$

where h is the topography in kilometers and g is the gravity in mGal. This expression arises because convective plumes typically give rise to an admittance value of around 50 mGal km^{-1} at long wavelengths [*McKenzie*, 1994]. The exact value of Z which is used has only a small effect on T_e, since the inclusion of a small long-wavelength topographic signal of convective origin will affect only the amplitude of flexural signals and not their characteristic wavelength. It is the latter which controls the determined value of T_e. Changing the value of Z by 10 mGal km^{-1} will typically alter the best fit value of T_e for a particular feature by 1–2 km.

[9] The gravity is calculated from the most recent spherical harmonic model, MGNP180U, which is tabulated to $l = m = 180$ [*Konopliv et al.*, 1999], and is low-pass filtered to retain only the long wavelength component. The filter function drops off to half its maximum value at a wavelength of 1000 km.

[10] Where there is zero in-plane force, the flexure of an elastic plate is described by

$$D\frac{d^4w}{dx^4} + \Delta\rho g w = 0, \tag{2}$$

where w is the vertical deflection of the plate, x is the horizontal distance perpendicular to the strike of the flexure, g is the acceleration due to gravity, $\Delta\rho$ is the density contrast between the mantle and the fluid overlying the plate, and D is its flexural rigidity.

$$D = \frac{ET_e^3}{12(1-\sigma^2)}, \tag{3}$$

where T_e is the thickness of the elastic plate, E is Young's modulus, and σ is Poisson's ratio (see Table 1).

[11] Over the range $x > 0$ for which no load is present, the general solution of (2) is of the form

$$w(x) = a_1 \exp\left(-\frac{x}{\alpha}\right)\cos\left(\frac{x}{\alpha}\right) + a_2 \exp\left(-\frac{x}{\alpha}\right)\sin\left(\frac{x}{\alpha}\right), \tag{4}$$

where the deflection is caused by a load which is applied to the plate at $x \leq 0$ and α is the flexural parameter

$$\alpha = \left(\frac{4D}{\Delta\rho g}\right)^{\frac{1}{4}}. \tag{5}$$

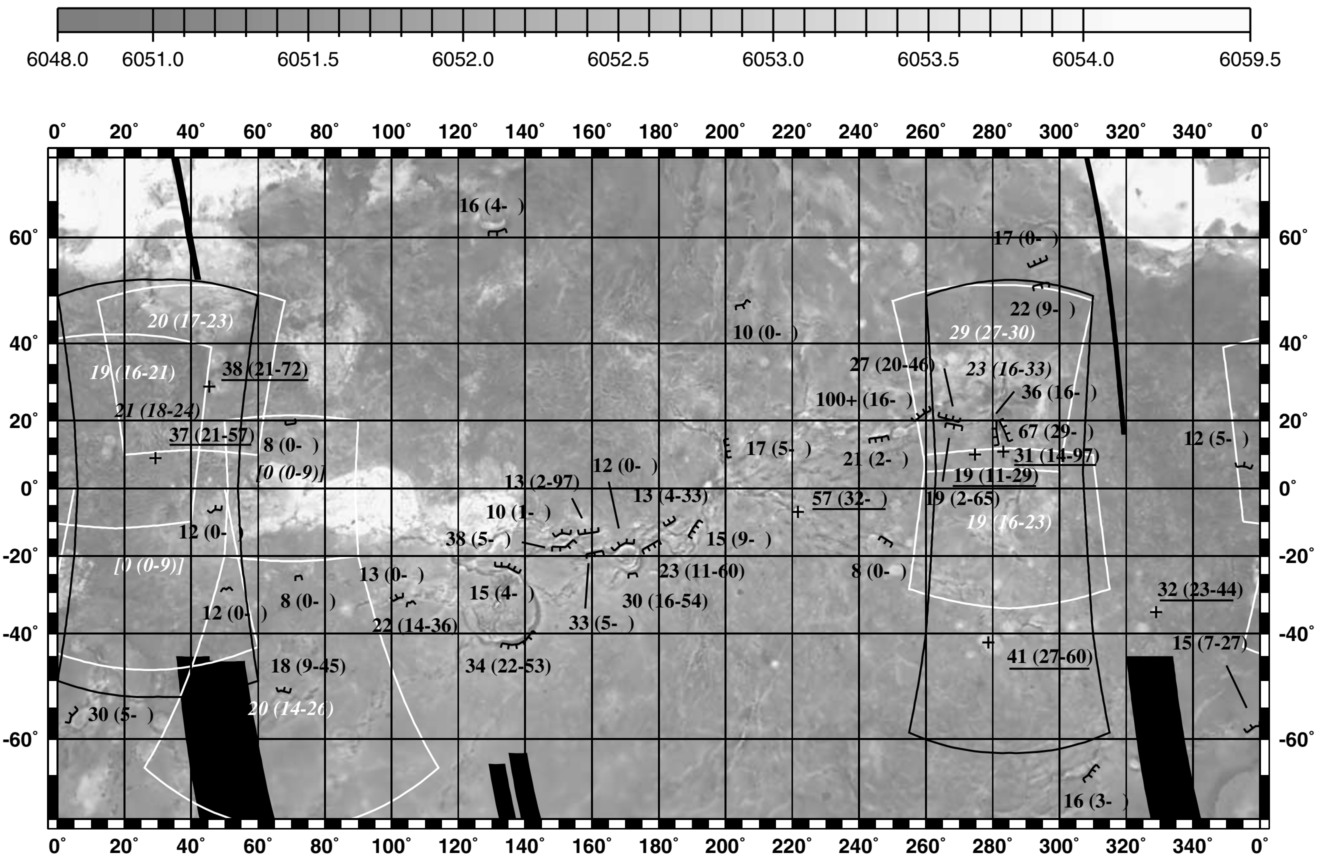

Figure 1. Residual topography of Venus in kilometers. The locations of the flexural profiles are shown by black lines, which follow the strike of the flexural features. These lines correspond to the ends of the profiles from which the average is calculated at each location. The tick marks show the direction in which the profiles are constructed. Also shown in each case is the best fit elastic thickness, in kilometers, for the average profile, together with the range of T_e over which the misfit is less than twice that at its minimum (in brackets) (see section 2 and Table 2). The features for which the elastic thickness was estimated by producing radial profiles through the spherical harmonic gravity [*Konopliv et al.*, 1999] are shown by crosses. For each of these features, the best fit elastic thickness, in kilometers, together with the range of T_e over which the misfit is less than twice that at its minimum (in brackets), is also shown (underlined) (see section 3 and Table 3). Shown for comparison are the best fit elastic thicknesses and their ranges within uncertainty (in brackets) obtained using line-of-sight accelerations for the boxes considered by *Barnett et al.* [2000] (italics). Note that the values for Ovda and Alpha (square brackets) are unreliable, because the topography is not well determined. The black areas are data gaps.

[12] In this study the observed deflection of the lithosphere is modeled using the expression

$$w(x) = a_1 \exp\left(-\frac{x}{\alpha}\right) \cos\left(\frac{x}{\alpha}\right) + a_2 \exp\left(-\frac{x}{\alpha}\right) \sin\left(\frac{x}{\alpha}\right), + a_3 x + a_4. \tag{6}$$

This expression represents the deflection of an elastic plate and also allows a bending moment to be applied to the end of the plate when $a_2 \neq 0$. In addition, the expression also allows a regional slope to be superimposed on the theoretical profile, because although the long-wavelength component of the topography due to dynamic support has been removed, any topographic slopes due to crustal thickening will still be present.

[13] For each location where flexure is to be modeled, a line is defined which is parallel to the strike of the flexural feature. Profiles are then produced at intervals of 10 km along this line, and perpendicular to it, in the direction in which the amplitude of the flexure decreases. An average profile is then calculated, in which the topographic height at each distance along the profile is defined as the mean of the heights of the real profiles at the same distance. Subsequently, the mean value of this average profile is set to zero. The mean value of each individual profile is then also set to zero, and the profiles are scaled linearly in the vertical direction such that their least squares misfit to the average profile is minimized. The standard deviation of the topographic values at each point along the average profile is then calculated. Such scaling changes the values of a_1 to a_4 which best fit the individual profiles, but not that of α (and hence T_e). The reason for averaging the profiles is to provide estimates of their standard deviation at each point, which is used to weight the misfit function. The effect of averaging T_e over the various profiles for any single feature is likely to be unimportant, since the area covered by the profiles for a given feature is small (<1000 km), and there are not likely to be significant variations in lithospheric parameters over such localized regions.

[14] For any given elastic thickness, and values for the parameters a_1, a_2, a_3 and a_4, a theoretical profile may be calculated as a function of distance x. The misfit H between this profile and the observed average profile may be calculated as follows

$$H^2 = \frac{1}{N} \sum_{n=1}^{N} \left[\frac{h_n - w(x_n)}{\sigma_n}\right]^2, \tag{7}$$

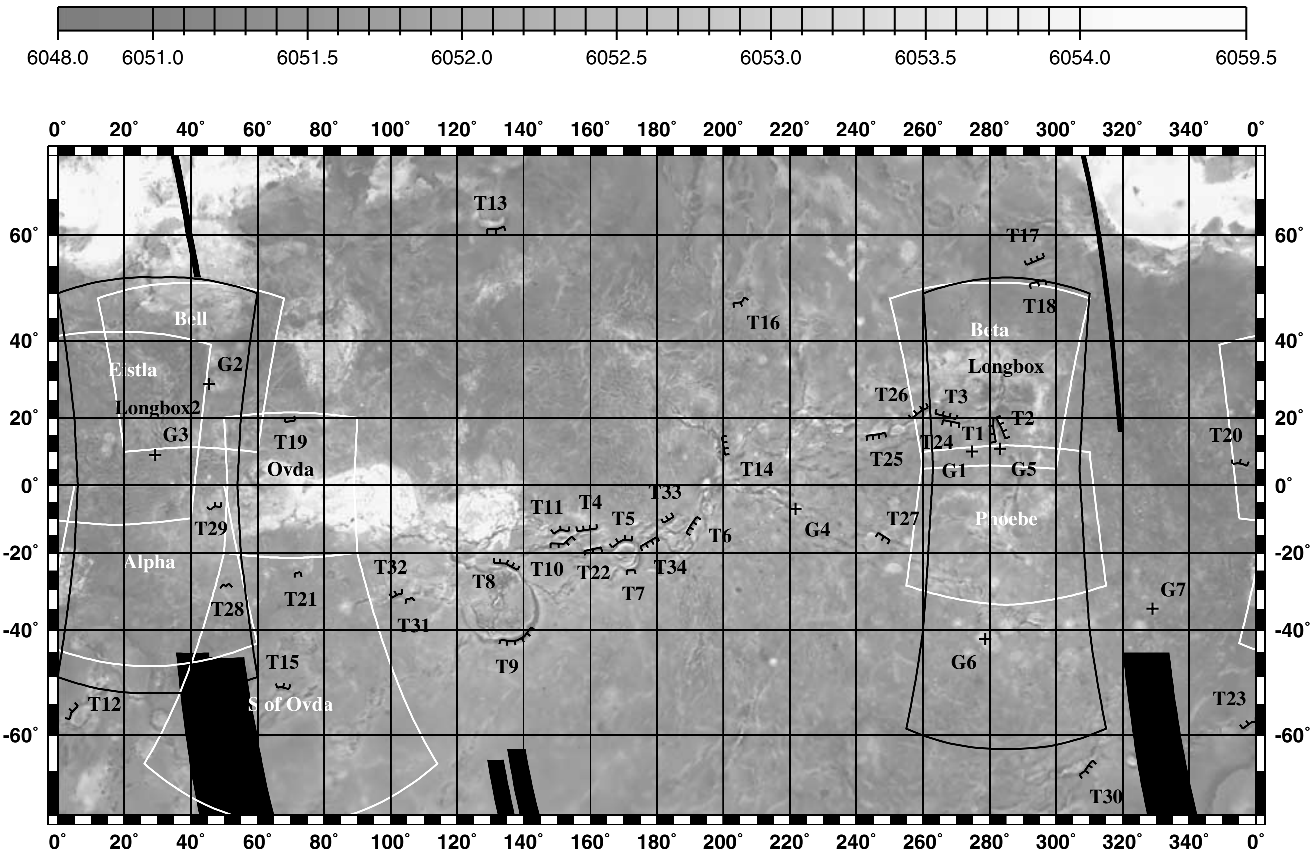

Figure 2. Residual topography of Venus in kilometers. The locations of the flexural profiles (section 2) are shown as in Figure 1, and the features modeled using the spherical harmonic gravity and the raw topography (section 3) are shown by crosses. The black areas are data gaps.

where $w(x_n)$ is as calculated in (6). The summation is over the number of points, N, in the mean profile, h_n is the topographic height of the nth point of the observed average profile, and σ_n is its standard deviation. The minimum misfit, and thus the best fit solution for the given value of the elastic thickness, occurs for some combination of values a_i (i = 1–4), such that all the partial derivatives $\partial H/\partial a_i$ are zero. Thus it is necessary to solve a set of simultaneous equations, which is achieved using singular value decomposition. The minimum misfit is then calculated as a function of the elastic thickness T_e. The minimum in this function will occur at the value of T_e which is the best fit to the data for the location of the particular profile in question.

[15] For any given profile, the bending moment $M(x)$ at a distance x along the profile is given by

$$M(x) = -D\frac{d^2w}{dx^2}, \tag{8}$$

from which the surface stress σ_{xx}may be calculated using

$$\sigma_{xx} = \frac{6M}{T_e^2}, \tag{9}$$

where a positive value indicates that the surface is in tension. The resulting shear stress is $\sigma_{xx}/2$.

2.2. Results

[16] The results for the 34 flexural features studied from the residual topography using a Cartesian model are shown in Figures 1 and 2 and Figure A1 and in Table 2. The misfit function is generally fairly flat over a large range of elastic thicknesses, because of the large number of parameters which can vary to achieve a best fit to the data, and increases at small values of T_e (typically in the region of 10 km). The elastic thickness is better constrained if a peripheral bulge is apparent in the topography (e.g., profiles T7, T9, T15, T23, T31, and T34).

[17] The method used in this work is such that the modeled profiles go flat (or have a linear slope) at their unflexed ends. The profile lengths were chosen such that any changes in slope at large distances from the feature being modeled, and which were deemed not to be flexural in origin, were not included in the modeling. In most cases, increasing the profile length does not have a large effect on T_e. If, however, profile T33 is lengthened, for example, the entire sloping section between distances of about 80 and 350 km from the start of the profile is interpreted as a flexural bulge, and thus the best fit value of T_e will be much higher.

[18] In this part of the work, a range of best fit elastic thicknesses was found, varying approximately 10 and 40 km or greater, with most in the range 10–20 km (see Figure 1). In general, the trends are consistent with those found by *Johnson and Sandwell* [1994] and *Sandwell and Schubert* [1992], although the values found in this work tend to be slightly smaller (typically by around 3–6 km) (see Table 2). Note that for a given value of α, the value obtained for T_e will depend on those assumed for E and σ. *Johnson and Sandwell* [1994] and *Sandwell and Schubert* [1992] use a value of 0.65 $\times$ 10^{11}Pa for E. This fact alone will yield elastic thicknesses which are around 15% higher than those obtained using our choice of parameter values, for a particular value of α. The values of T_e found in this work are also slightly smaller than estimates obtained using LOS accelerations in the frequency domain [*Barnett et al.*, 2000; *McKenzie and Nimmo*, 1997], which

Table 2. Flexural Profiles (Residual Topography)

Profile	Physical Feature	Location	Best Fit T_e,[a] km	Previous Values, km
T1	North Devana Chasma (west side)	17°N, 281°E	36 (16–)	
T2	North Devana Chasma (east side)	17°N, 284°E	67 (29–)	
T3		20°N, 267°E	27 (20–46)	
T4	East Diana Chasma	13°S, 159°E	13 (2–97)	
T5	East Dali Chasma	17°S, 169°E	12 (0–)	
T6		12°S,190°E	15 (9–)	
T7	Latona Corona	25°S, 172°E	30 (16–54)	35[b]
T8	North Artemis Corona	24°S, 134°E	15 (4–)	
T9	South Artemis Corona	41°S, 138°E	34 (22–53)	37[b]
T10	West Diana Chasma	16°S, 151°E	38 (5–)	
T11		14°S,151°E	10(1–)	
T12	Eithinoha	56°S, 4°E	30 (5–)	15[b]
T13	Nightingale Corona	61°N, 132°E	16 (4–)	22[c]
T14	Ganis Chasma	12°N, 200°E	17 (5–)	
T15		52°S, 67°E	18 (9–45)	
T16	Neyterkob Corona	49°N, 205°E	10 (0–)	14[c]
T17	North Demeter Corona	56°N, 294°E	17 (0–)	24[c]
T18	South Demeter Corona	52°N, 294°E	22 (9–)	22[c]
T19	"Ridge"	19°N, 70°E	8(0–)	18[c]
T20	Heng-O Corona	6°N, 355°E	12(5–)	40[b]
T21	Nishtigri Corona	26°S, 72°E	8 (0–)	12[c]
T22	West Dali Chasma	19°N, 161°E	33(5–)	34[c]
T23	Kalaipahoa Linea	58°S, 358°E	15 (7–27)	
T24		19°N, 268°E	19 (2–65)	
T25	West Hecate Chasma	15°N, 246°E	21 (2–)	
T26	E Hecate Chasma	21°N, 259°E	100+ (16–)	
T27	Parga Chasma	15°S, 248°E	8 (0–)	
T28		29°S, 50°E	12 (0–)	
T29	Nabuzana Corona	7°S, 47°E	12 (0–)	
T30	Morrigan Linea	64°S, 105°E	16 (3–)	
T31	East Juno Chasma	32°N, 105°E	22 (14–36)	
T32	West Juno Chasma	31°N, 102°E	13 (0–)	
T33	Zemina Corona	10°N, 183°E	13 (4–33)	
T34		17°N, 177°E	23 (11–60)	

[a] Shown in brackets is the range of T_e over whcih the misfit function is less than twice that at its minimum, as a guide to the uncertainty. Where no upper limit is given, this indicates that this upper limit is > 100 km. Where the best fit value of T_e is > 100 km, the lower limit is calculated as the elastic thickness at which the misfit is twice that at a T_e of 100 km.
[b] *Sandwell and Schubert* [1992].
[c] *Johnson and Sandwell* [1994].

tend to be in the range 20–30 km. This is in agreement with conclusions reached by *McKenzie and Nimmo* [1997].

[19] Overall, however, there is no convincing evidence for any regional variations in T_e. The average elastic thickness over the whole region studied, weighting the values according to the inverse of the squares of their ranges of uncertainty, is ∼25 km, which falls within the bounds of uncertainty of T_e for almost all the locations studied. In fact, the plots in Figure A1 show also the best fit theoretical profile in each case, assuming the elastic thickness is 25 km. As the misfit functions suggest, the fits to the observed profiles are degraded only slightly when compared to those for the best fit elastic thicknesses; the profiles for which T_e is constrained to be 25 km provide fits to within the standard deviation of the average observed profiles in almost all cases. There is, however, a suggestion, based on the geographical distribution best fit values of T_e (Figure 1), that the region around Beta Regio and the rifts on the south side of Artemis, Diana, and Dali Chasmata may exhibit higher elastic thicknesses than elsewhere.

[20] An estimate of the maximum stress σ_s along each profile is given by the first extremum of $\sigma_s(x)$ for $x > 0$, rather than by the extreme value at $x = 0$, which results from the assumptions of the fitting process. Equation (6) assumes that all topography associated with the load is confined to the region $x \leq 0$ and that where $x > 0$, the surface would be horizontal in the absence of the load. However, there is no obvious way of choosing the origin of the profile being fitted so that it is on the edge of the load. We fitted profiles which resembled those expected from flexure and chose the origin to be beyond what we thought was the load. If, however, any of the topography where $x > 0$ is not due to flexure, artificially large stresses result when it is fitted by the plate-bending model. Such errors have little effect on the misfit H because only a small fraction of the length of the profile is affected. Thus the maximum shear stresses which are imposed on the plate are of the order of a few hundreds of MPa. This is greater than the 80 MPa or so which faults on Venus are believed to be able to withstand [*Foster and Nimmo*, 1996], which is consistent with the surface faulting visible in the synthetic aperture radar (SAR) images at many of the locations studied.

3. Flexure Measured From Gravity Using Raw Topography

3.1. Introduction and Method

[21] The most recent spherical harmonic gravity model of Venus extends to $l = m = 180$ [*Konopliv et al.*, 1999]. *Barnett et al.* [2000] showed that the spherical harmonic coefficients corresponding to wavelengths less than ∼500 km (where $k = 2\pi/\lambda = (l + (1/2))/a$) are systematically too small, because the signal-to-noise ratio at short wavelengths is too low to allow the spherical harmonic gravity field to be accurately calculated. An a priori constraint is imposed on the coefficients such that they are constrained toward zero (with an uncertainty given by Kaula's rule [*Kaula*, 1966]) for all degrees where the noise in the data exceeds the signal [*Konopliv et al.*, 1999]. The effect of this constraint may be shown by calculating

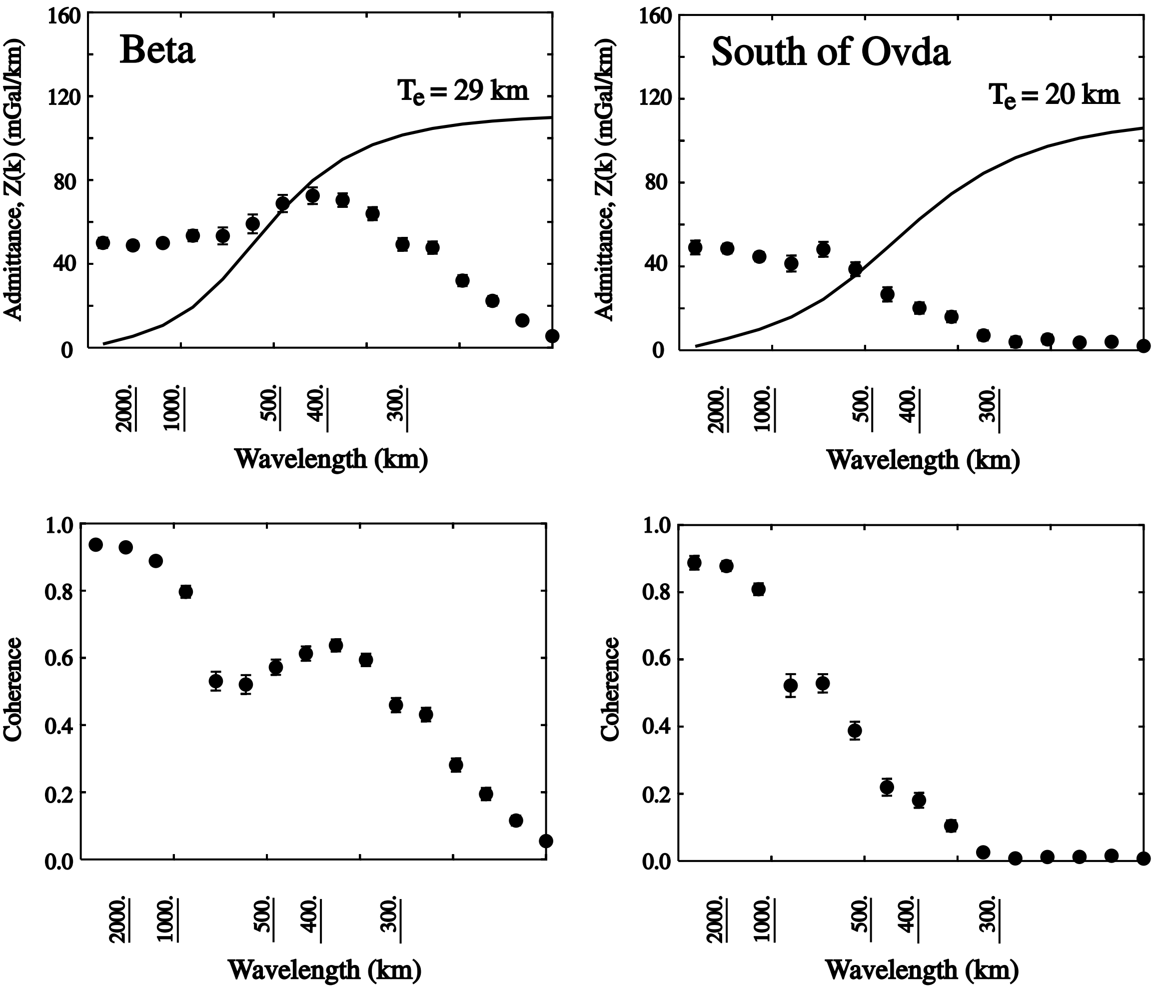

Figure 3. Plots of the two-dimensional (2-D) admittance and coherence for the "Beta" and "South of Ovda" boxes (as shown in Figure 2), using raw topography as the input and the spherical harmonic gravity (to $l = m = 180$) as the output. Also shown is the theoretical admittance curve for the best fit elastic thickness, calculated using the admittance between calculated and observed gridded LOS accelerations for each box [*Barnett et al.*, 2000].

the admittance as a function of wave number $Z(k)$ from the gridded spherical harmonic gravity and the raw topography, as shown for the box containing Beta in Figure 3. (The location of this box is shown in Figure 2.) At long wavelengths the admittance calculated using the spherical harmonic gravity is $\sim$50 mGal km^{-1}, in agreement with the value calculated using the line-of-sight accelerations and corresponding to dynamic support of the topography [*Barnett et al.*, 2000]. At wavelengths shorter than $\sim$500 km, the admittance calculated using the spherical harmonics drops off to zero. Conversely, the admittance calculated from the LOS accelerations for the same box increases at short wavelengths and allows the elastic thickness to be constrained [*Barnett et al.*, 2000], because the signal processing is able to extract information even when the signal-to-noise ratio is low. However, even with the spherical harmonic gravity, the admittance drops off only gently, and the coherence remains high down to wavelengths as short as 250 km. The high coherence suggests that although the amplitude of the gravity signals is inaccurate, their shape is correct, and thus the gravity may be used for flexural modeling, if the effect of the a priori constraint is taken into account.

[22] We assumed that the admittance values, and hence the elastic thickness, calculated from the LOS accelerations [*Barnett et al.*, 2000] are correct, and thus the theoretical admittance curve for this value of T_e gives the expected value for the admittance for each wave number. The drop-off of the observed values of the spherical harmonic admittance at short wavelengths is modeled using a smooth (Gaussian) function, $Z(k)_{sphharm}$, where

$$Z(k)_{sphharm} = A \exp\left(\frac{-\left(k - \mu_f\right)^2}{2\sigma_f^2}\right). \tag{10}$$

In the case of the "Beta" box, $A = 73$ mGal km^{-1}, $\mu_f = 1.53 \times 10^{-5}$ m^{-1}, and $\sigma_f = 0.7 \times 10^{-5}$m^{-1}. It is then possible to construct a filter function $f(k)$, the value of which at any wave number k is given by

$$f(k) = \begin{cases} Z(k)_{sphharm} \big/ Z(k)_{LOS} & Z(k)_{sphharm} < Z(k)_{LOS} \\ 1 & \text{otherwise} \end{cases}, \tag{11}$$

where $Z(k)_{LOS}$ is the value of the admittance curve which is a best fit to the LOS admittance data. The function $f(k)$ therefore represents the factor by which the gravity coefficients have been reduced by the effect of the a priori constraint imposed on them (see Figure 4). Therefore a theoretical gravity model can be convolved with this filter function and the misfit between the

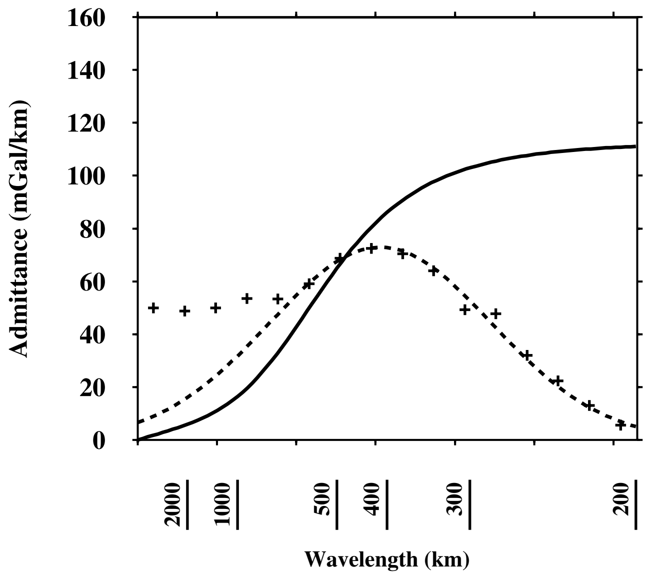

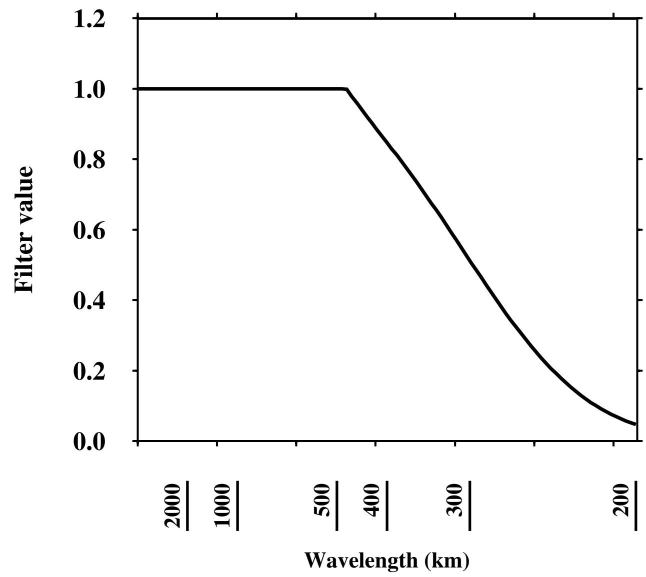

Figure 4. (top) The admittance calculated from the topography and spherical harmonic gravity (crosses), together with the theoretical admittance curve, $Z(k)_{LOS}$ (solid black line) for the Beta box, as in Figure 3. $Z(k)_{sphharm}$, the Gaussian function which is used to fit the observed admittance at short wavelengths, is shown as a dashed line. (bottom) The filter function which is produced, as a function of wavelength.

theoretical model and the observed spherical harmonic gravity can then be calculated.

[23] In equatorial regions the spherical harmonic gravity model contains information derived mostly from Magellan mapping cycle 4, during which the spacecraft altitude was lower than at any other point in the mission. During this cycle the spacecraft orbit was approximately polar, with a periapse at ~10°N, and the spacecraft altitude was roughly constant at constant latitudes. Therefore the filter derived from the box containing Beta will be likely to be applicable to the spherical harmonic gravity for any location within a similar latitude band.

[24] Several Venusian volcanoes have features resembling flexural moats surrounding them, which are visible in the spherical harmonic gravity model (see Figure 5). It is these features which were modeled for this part of the study. Note that there are also artefacts visible in the gravity, which appear as straight lines when projected on a polar plot. These result from noise on the corresponding orbit tracks and mostly affect the higher-order terms between approximately l = 150 and l = 180 (A. S. Konopliv, personal communication, 2000). These artefacts are of similar amplitude to the features we wish to model. We reduced this and other sources of noise by producing a series of radial profiles, centered on the feature under consideration, constructed through a range of azimuths over which the flexural moat is clearly defined and the gravity field beyond is relatively flat. Adjacent profiles differed in azimuth by 10°. An average profile and the standard deviation of the gravity at each point were then calculated in the same way as was done for the residual topographic profiles (section 2). Note that the grids from which these profiles were produced used an Airy projection [*Snyder*, 1989], rather than the equidistant cylindrical projection used for Figure 5, with a pole roughly in the center of the plot in each case, to minimize length and angular distortion.

[25] An average topographic profile was then produced, from a series of radial profiles of the gridded raw topography, over the same range of azimuths as for the gravity. Since the problem is cylindrically symmetric, the topography $h(r)$ can be expressed as a Bessel function series:

$$h(r) = \sum_{m=1}^{50} A_m J_0\left(k_m \frac{r}{r_{\max}}\right), \tag{12}$$

where k_m is the value of the mth root of the Bessel function J_0 and r_{max} is the length of the radial profiles. The gravity as a function of radius was then calculated for a range of elastic thicknesses T_e by convolving the topography with the product of the admittance function $Z(k_m)$ and the filter function $f(k_m)$ (equation (11)). $Z(k_m)$ is given by

$$Z(k_m) = 2\pi G(\rho_c - \rho_w)\left[1 - \exp\left(-k_m t_c\right)\left(1 + \frac{Dk_m^4}{(\rho_m - \rho_c)g}\right)^{-1}\right], \tag{13}$$

where G is the gravitational constant, ρ_m, ρ_c, and ρ_w are the densities of the upper mantle, the crust, and the overlying fluid, respectively, and t_c is the thickness of the crust, as given in Table 1. This expression is the same as that for the Cartesian problem, apart from the replacement of the wave number, $(k_x^2 + k_y^2)^{1/2}$, with k_m. The choice of value for t_c is discussed in section 3.2.

[26] Note that (13) assumes a "top-loading" model for the elastic plate (a value of f, the ratio of subsurface loading to surface loading, equal to 0). The justification for this assumption is that the density contrast associated with surface loads (i.e., between rock and air) is likely to be far greater than the density contrast produced by subsurface loading (e.g., Moho topography), so the effects of surface loading are likely to be dominant [see *McKenzie and Fairhead*, 1997]. This assumption is likely to be correct on Venus, where the crust is volcanic throughout and features such as sedimentary basins are absent, such that there are likely to be few lateral density contrasts within the crust.

[27] For each value of T_e, a constant offset Δg of the calculated gravity profile with respect to the observed profile was varied to minimize the misfit H between these profiles.

$$H^2 = \frac{1}{N}\sum_{n=1}^{N} r_n \left[\frac{g_o^n - g_c^n}{\sigma_n}\right]^2, \tag{14}$$

where the summation is over the number of points, N, in the profiles, $g_c{}^n$ and $g_o{}^n$ are the values of the gravity at the nth points of

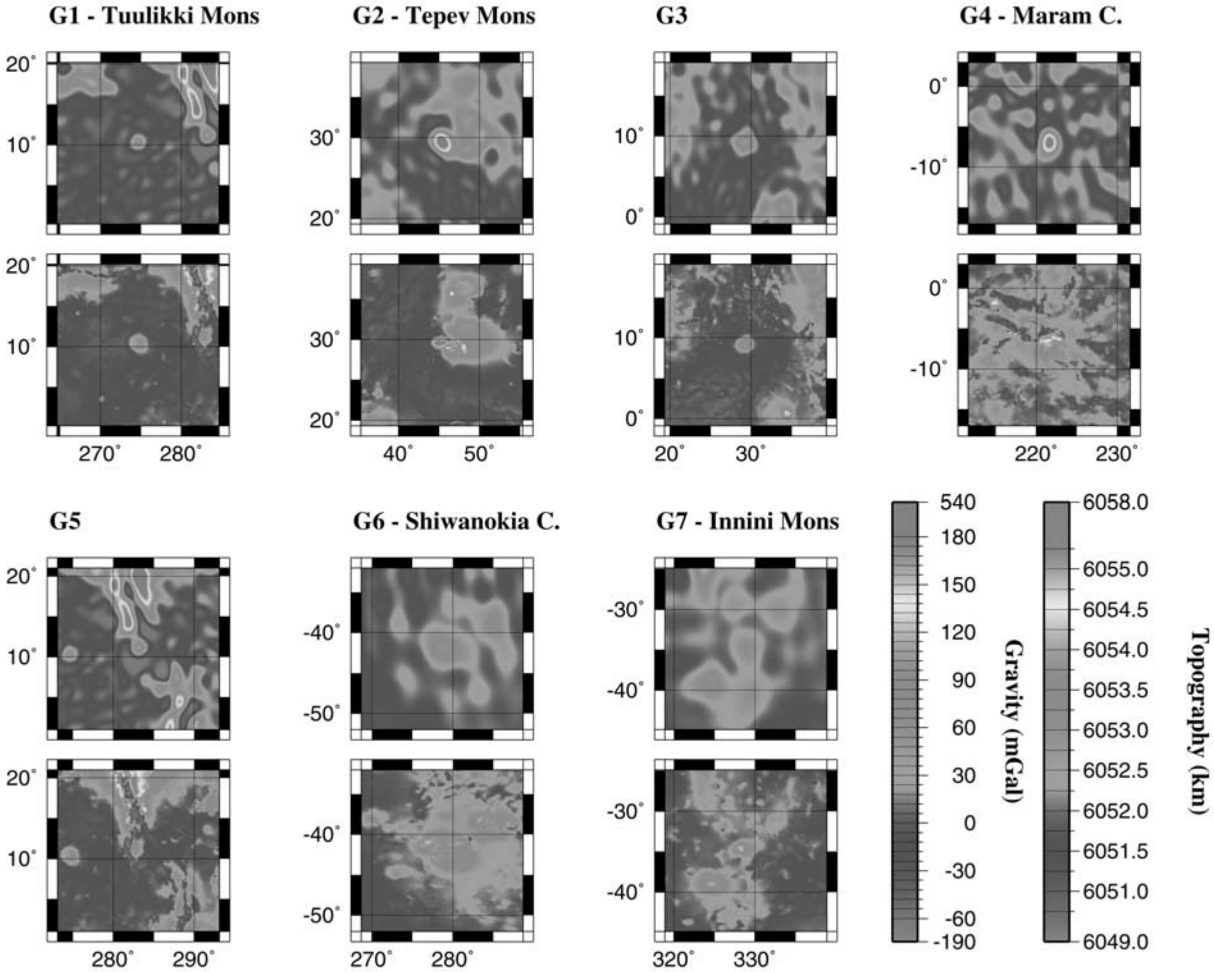

Figure 5. Venus gravity in mGal, calculated from the spherical harmonic model to $l = m = 180$ [*Konopliv et al.*, 1999] (top plots) and raw topography (bottom plots), for the locations of the seven features (center of each box) from which radial profiles were calculated and the elastic thickness was estimated. See color version of this figure at back of this issue.

the calculated and observed profiles, respectively (at radial distance r_n from the center of the feature), and σ_n is the standard deviation of the gravity at the nth point of the observed average profile. Note that the misfit is weighted by the radial distance r_n since the misfit is effectively being calculated over an annulus of circumference $2\pi r_n$. The misfit is therefore not dimensionless, but has units km$^{-1/2}$. The misfit is calculated for $r \leq r_o$, where r_o is the radius of the edge of the flexural moat observed in the gravity profiles.

3.2. Results

[28] The elastic thicknesses calculated from the gravity and topography profiles are generally better constrained than the values calculated by modeling the residual topography alone (section 2). The best fit values range from around 20 to 60 km (see Figures 1 and A2 and Table 3). However, the plots of $H(T_e)$ show that the estimates of T_e are not sufficiently well-constrained to show any convincing regional variations. As for the residual topographic profiles (section 2), all profiles are well fit by an elastic thickness of 25 km.

[29] If all the synthetic gravity profiles are calculated similarly, the fits to profiles G6 and G7 are much poorer than to the other five profiles, and the minimum misfits are higher. The reason for this is probably that features G6 and G7 are farther south than the others, and thus the gravity filter, which was produced by considering the results for the Beta box, is not applicable at these higher latitudes. The synthetic profiles G6 and G7 were therefore recalculated using a gravity filter calculated from the "South of Ovda" box (see Figure 1) (between latitudes of 70°S and 20°S) (see Figure 6), which greatly improves the fits (see Figure A2b). For this filter the terms in (10) are $A = 60$ mGal km^{-1}, $\mu_f = 0.2 \times 10^{-5}$ m^{-1}, and $\sigma_f = 0.9 \times 10^{-5}$m^{-1}. Figure 3 shows the admittance calculated from the spherical harmonic gravity and the raw topography for this box and shows that $Z(k)$ decreases monotonically with increasing k. In addition, the coherence drops off at longer wavelengths than for Beta. However, the observed coherence between wavelengths of 300 and 500 km is still of order 0.1, and the theoretical gravity profiles calculated using the filter in Figure 6 show central maxima, which can only be explained by elastic support of the observed topography. The resolution in the gravity field, even at these higher latitudes, is therefore good enough to allow $T_e$to be estimated, though less accurately than at lower latitudes.

[30] The assumed value for t_c (see equation (13) and Table 1) in this work was 16 km, which is somewhat smaller than the crustal thickness estimates of 25–30 km given by some previous authors [e.g., *Grimm and Hess*, 1997; *Kiefer and Potter*, 2000]. There is some trade-off between the assumed value of $t_c$and the best fit T_e. However, increasing t_c from 16 to 30 km does not change the best fit elastic thickness by more than 5 km for any of the features studied. In any case, t_c represents the effective depth of compen-

Table 3. Flexural Profiles (Gravity and Raw Topography)

Profile	Physical Feature	Location	Azimuth Range,[a] deg	Best Fit T_e,[b] km		Previous Values, km
				"Beta" Filter	"S of Ovda" Filter	
G1	Tuulikki Mons	10°N, 275°E	10–360	19 (11–29)		8[c]
G2	Tepev Mons	29°N, 45°E	180–360	38 (21–72)		
G3		9°N, 29°E	10–360	37 (21–57)		
G4	Maram Corona	7°S, 222°E	10–360	57 (32–)		
G5		11°N, 283°E	10–360	31 (14–97)		
G6	Shiwanokia Corona	42°S, 279°E	10–360		41 (27–60)	
G7	Innini Mons	35°S, 329°E	10–360		32 (23–44)	17[c]

[a] Range of azimuths over which the individual radial profiles were constructed.
[b] Shown in brackets is the range of T_e over which the misfit function is less than twice that at its minimum, as a guide to the uncertainty. Where no upper limit is given, this indicates that this upper limit is >100 km. The values shown in the right-hand subcolumn are those calculated using the gravity filter derived from admittance analysis of the "South of Ovda" box (see Figures 3 and 6). This filter is likely to be more appropriate for profiles G6 and G7.
[c] *Kiefer and Potter* [2000].

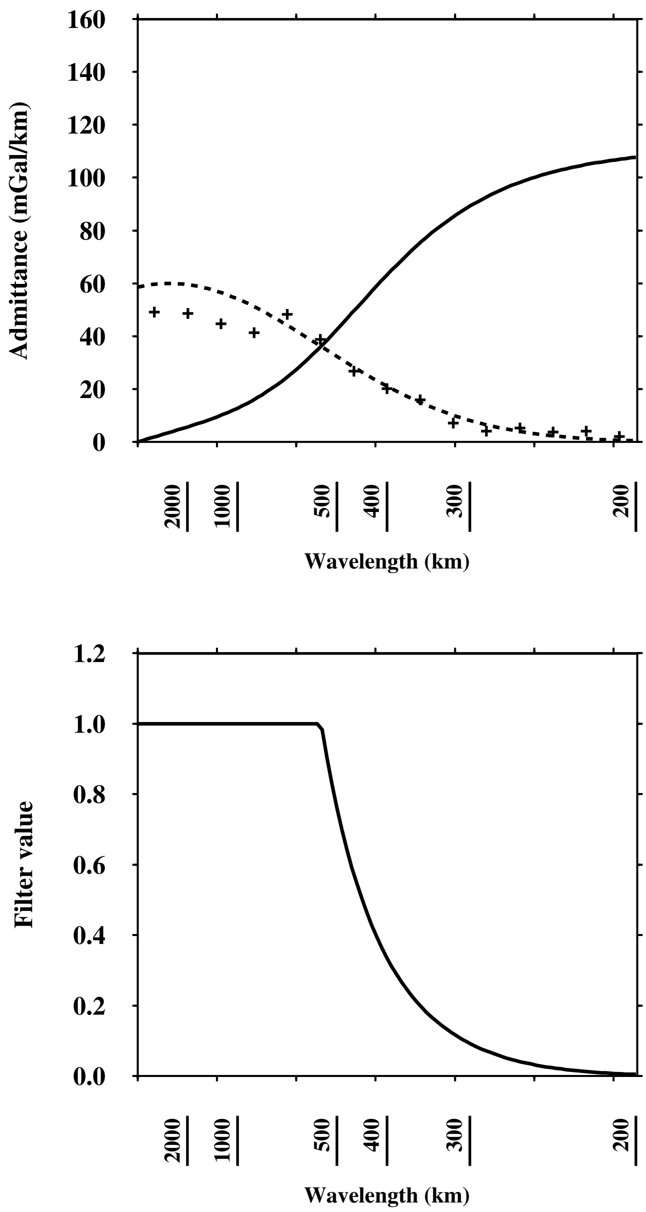

Figure 6. As Figure 4, but for the South of Ovda box (see Figure 2).

sation, which is likely to be smaller than the crustal thickness, since the Venusian crustal density is likely to increase with depth (rather than be uniform throughout), as is the case in volcanically generated crust on Earth.

4. Discussion and Conclusions

[31] Where flexure of residual topography alone is modeled (section 2), the constraint on T_e is relatively poor, often giving only a lower limit below which the fits to the observed data are less good. Thus, although a range of elastic thickness estimates between approximately 10 and 40 km was found, an elastic thickness of 25 km allows all profiles to be fit within uncertainty. Both the stacked profiles used in this work and profiles which are

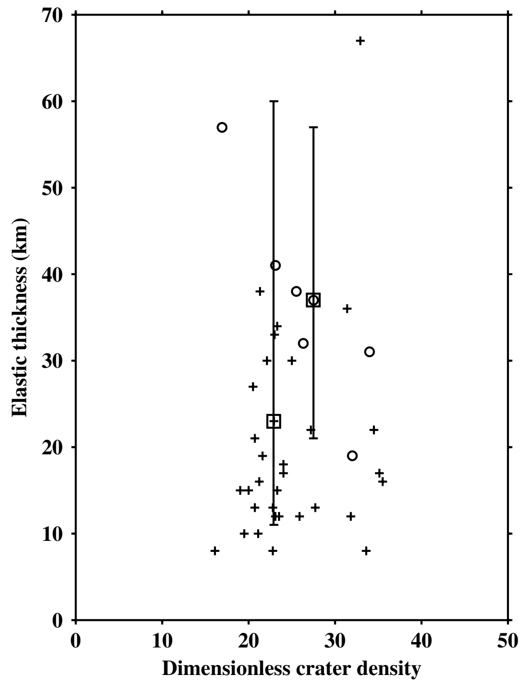

Figure 7. Plot of the elastic thickness estimates obtained by flexural modeling of residual topography (crosses) (section 2) and modeling of gravity using the observed topography (circles) (section 3) against dimensionless crater density at the same locations, obtained using a Gaussian window of standard deviation 1000 km. Note that for the two boxed data points, error bars corresponding to the range of T_e over which the misfit is less than twice that at its minimum are shown, as representative examples.

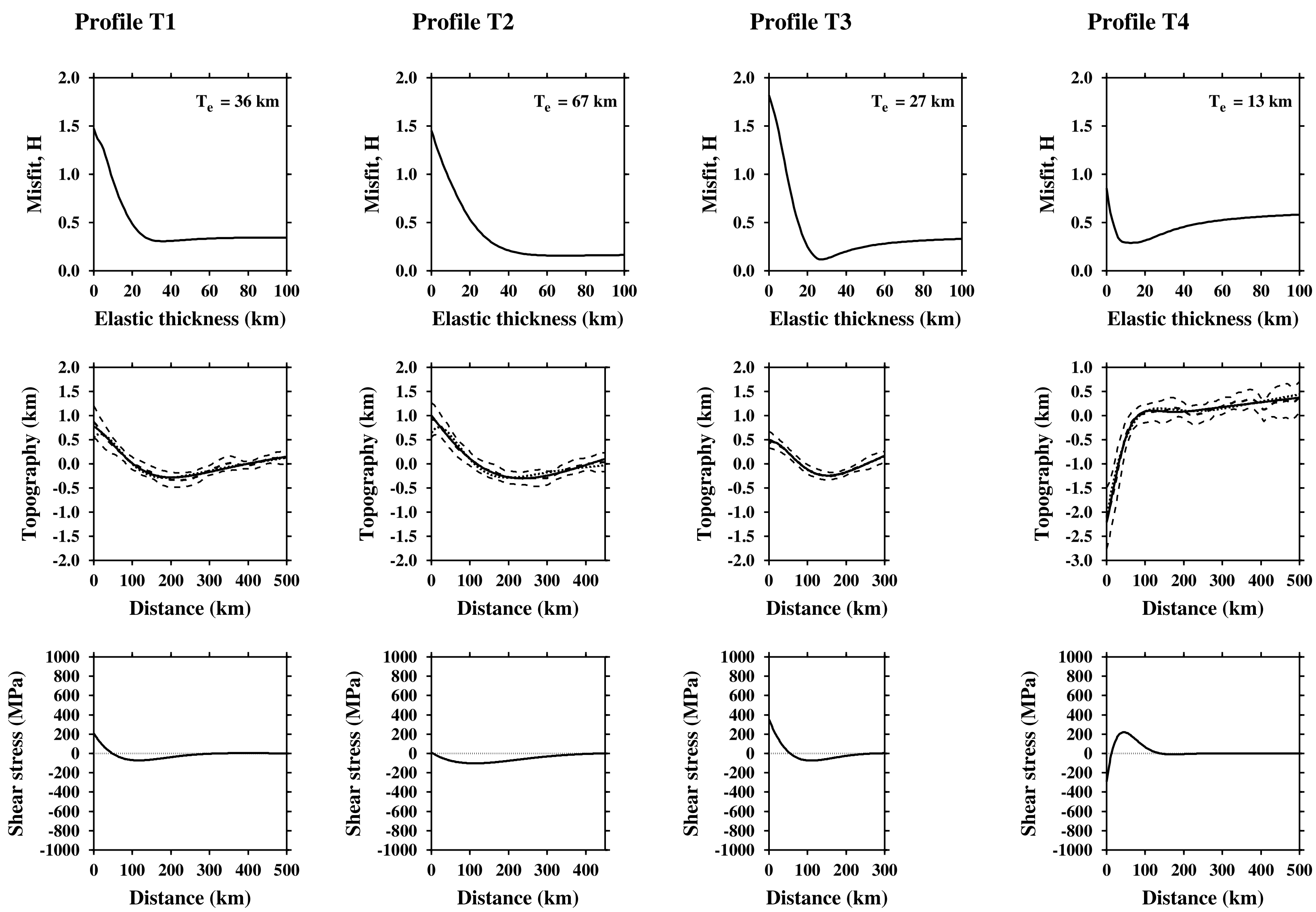

Figure A1. Results for the 34 profiles (T1–T34) constructed from the residual topography. The center plots show the average topographic profile in each case (dashed line), and the lines above and below (thin dashed lines) show the topography plus and minus (respectively) its standard deviation at each point. The top plots show the minimum misfit between the calculated and observed profiles, as a function of elastic thickness. The mimima in these curves give the best fit elastic thickness for each location, which is used to calculate the best fit profile, shown in the center plot as a solid line. The lower plots show the shear stress, calculated as a function of distance along the profile. Also shown in the center plot in each case is the best fit calculated profile, assuming an elastic thickness of 25 km (dotted line).

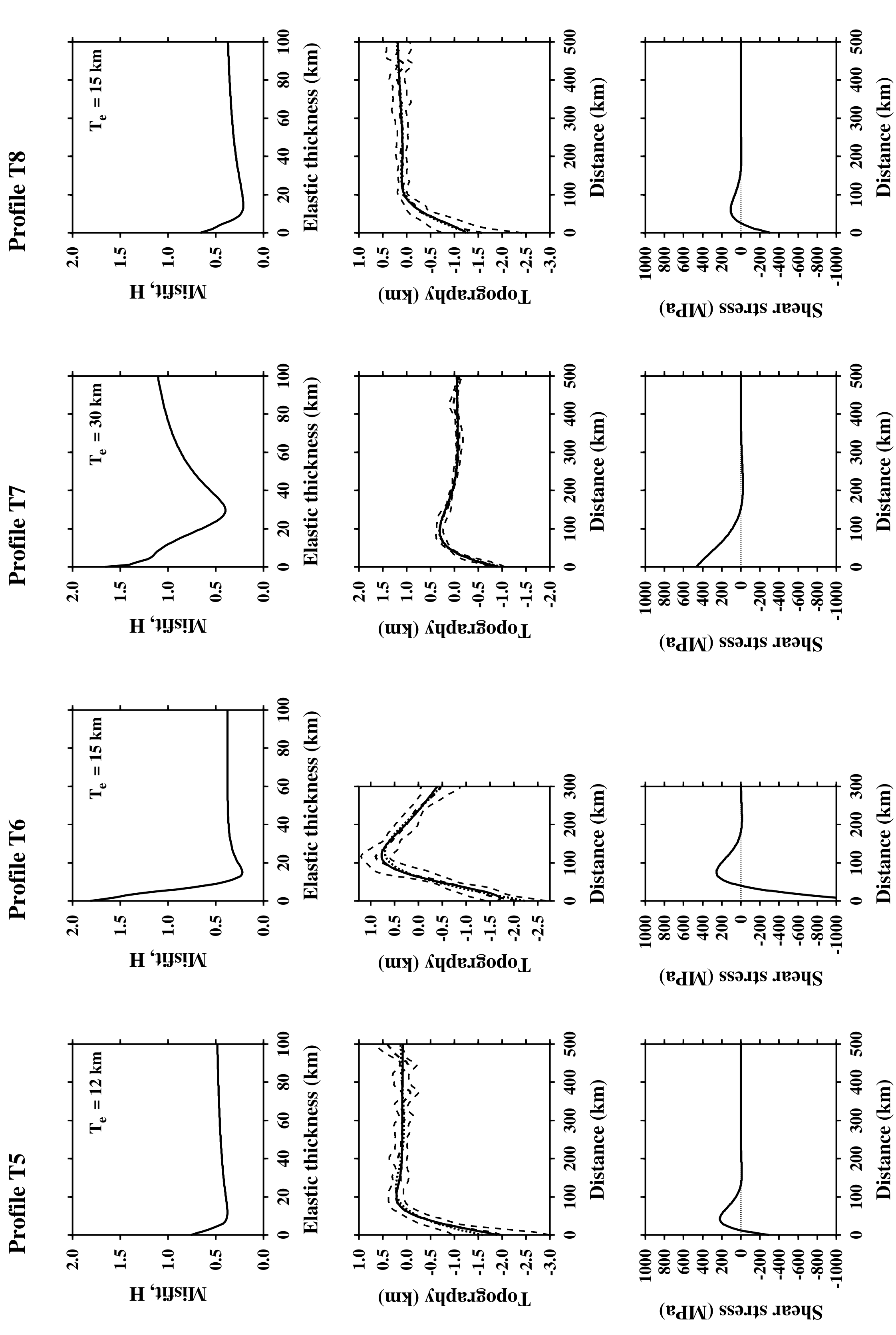

Figure A1. (continued)

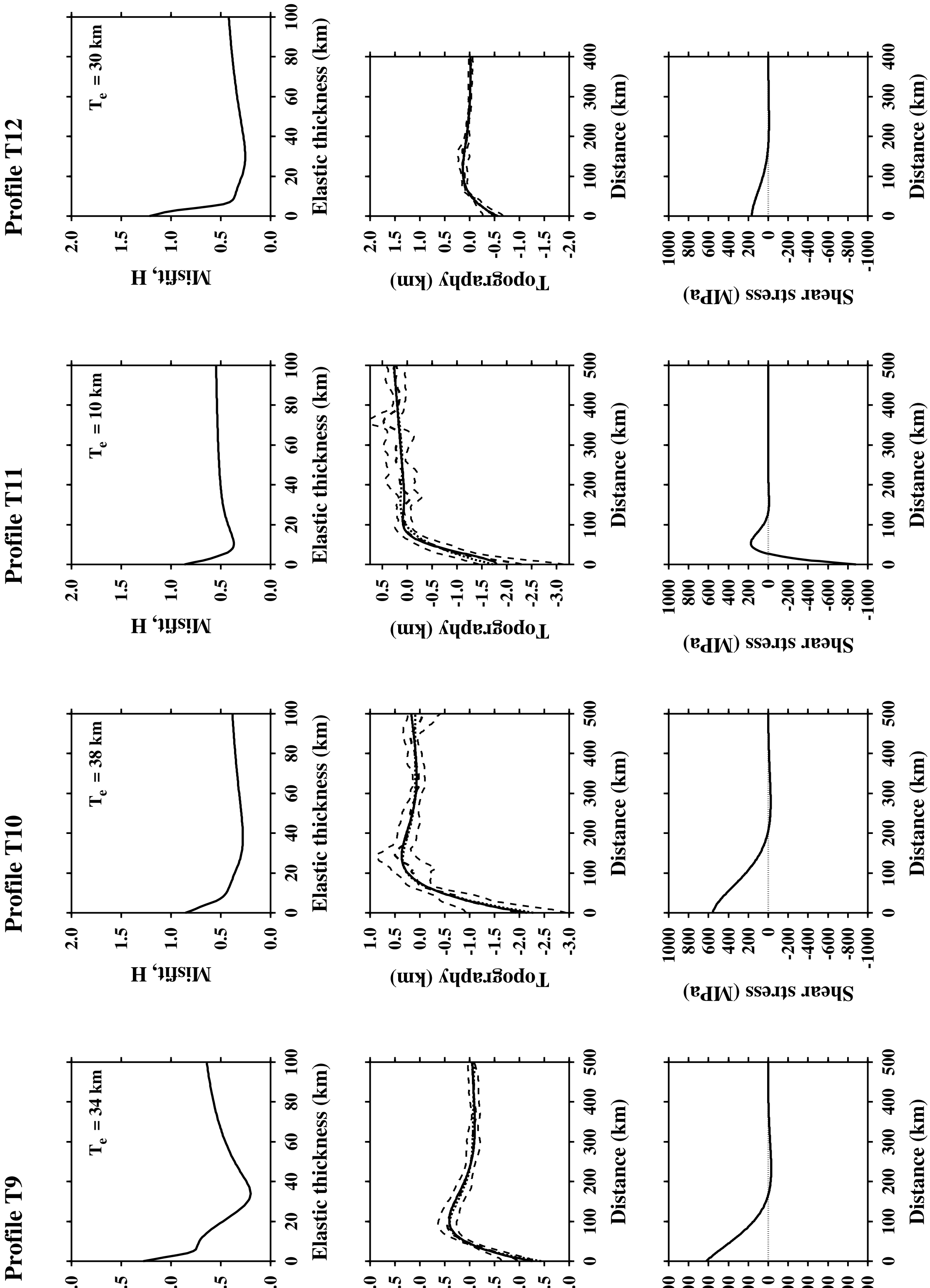

Figure A1. (continued)

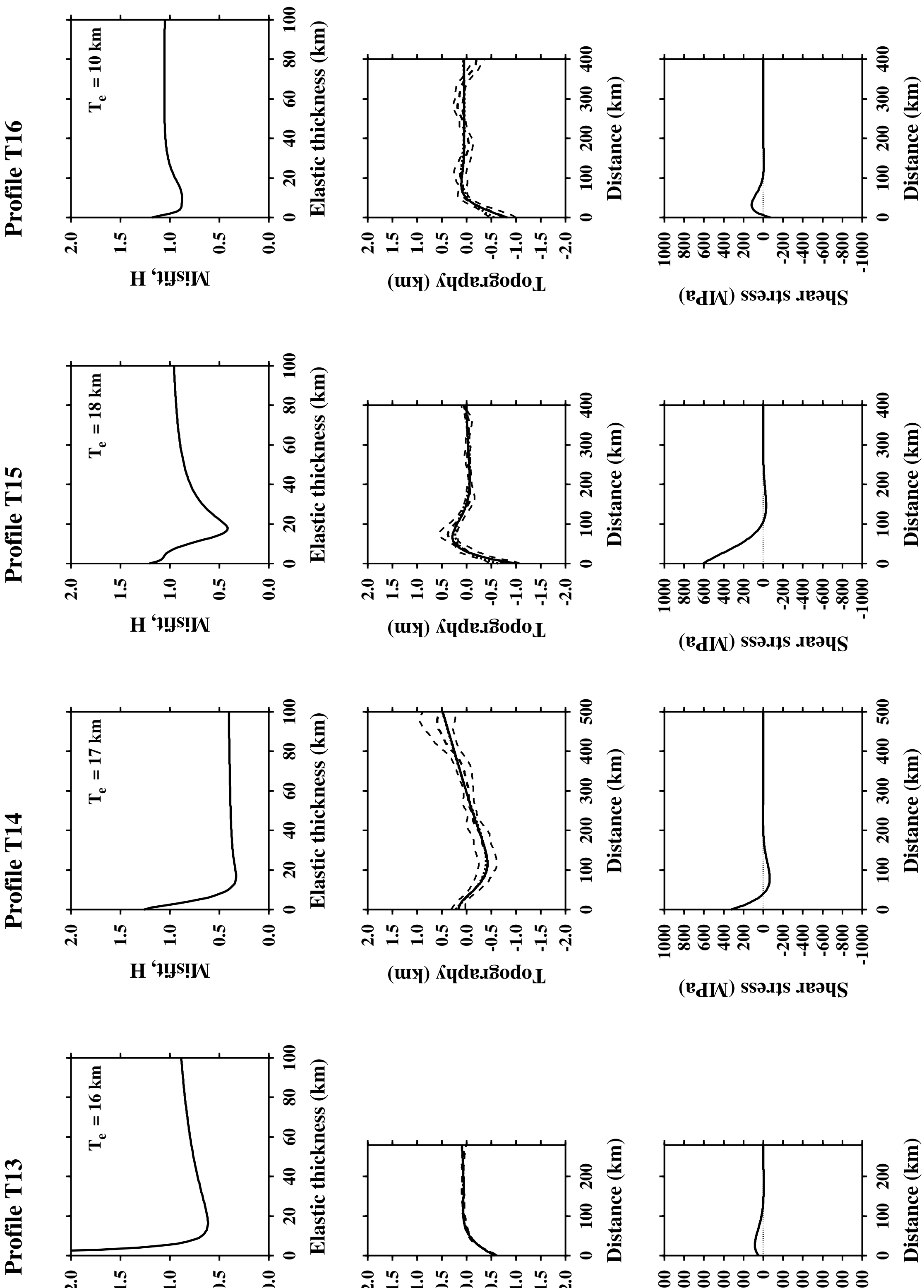

Figure A1. (continued)

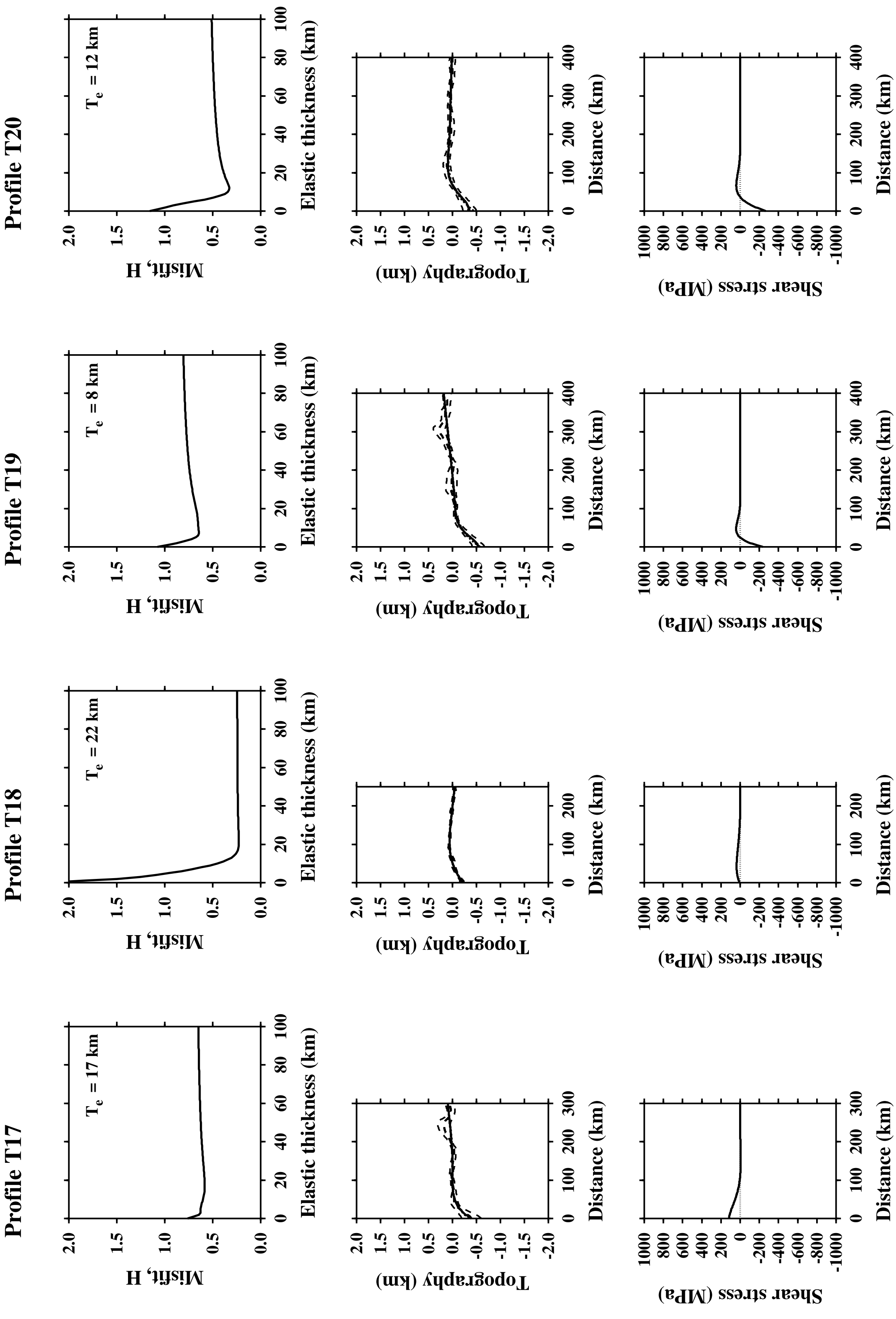

Figure A1. (continued)

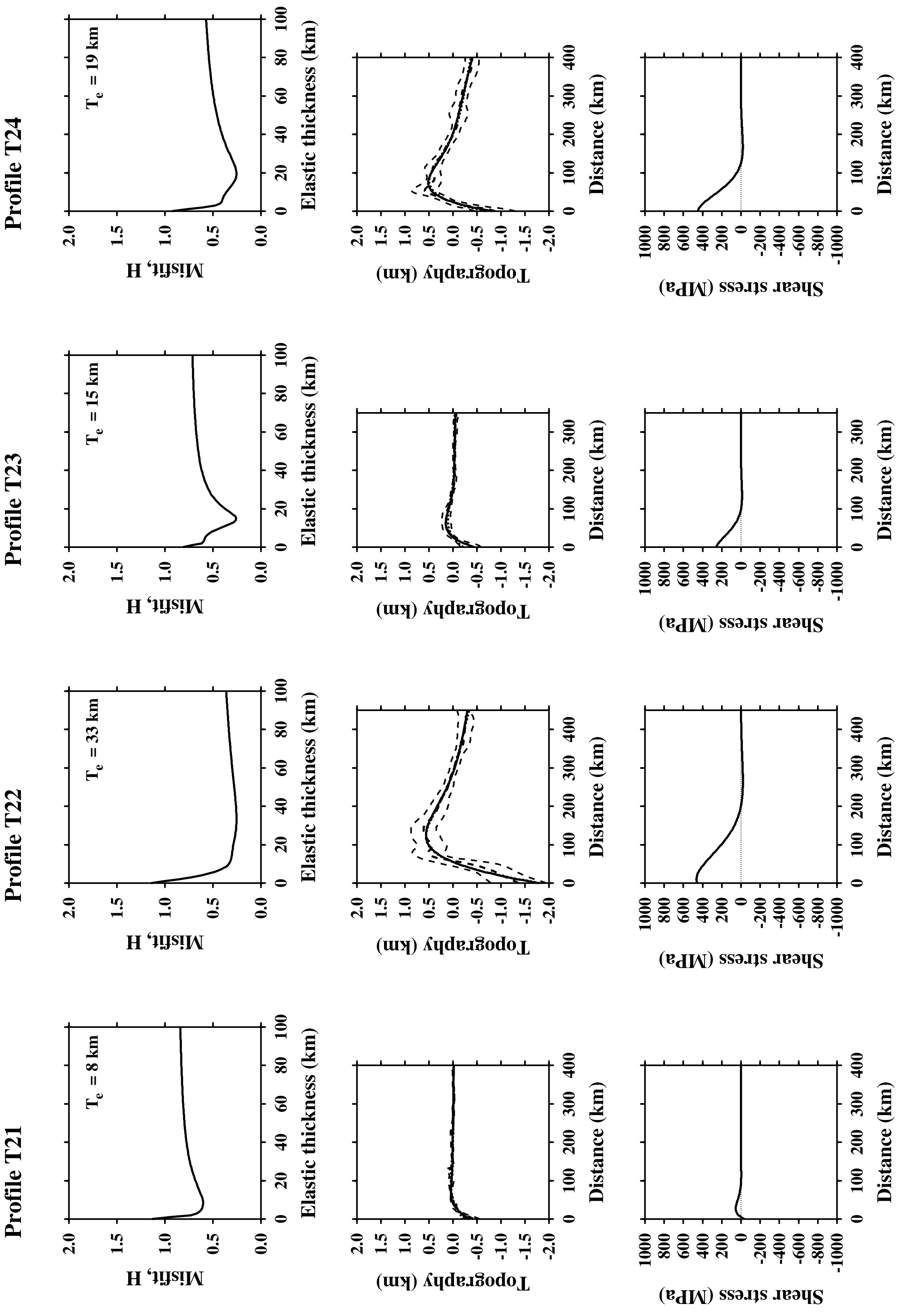

Figure A1. (continued)

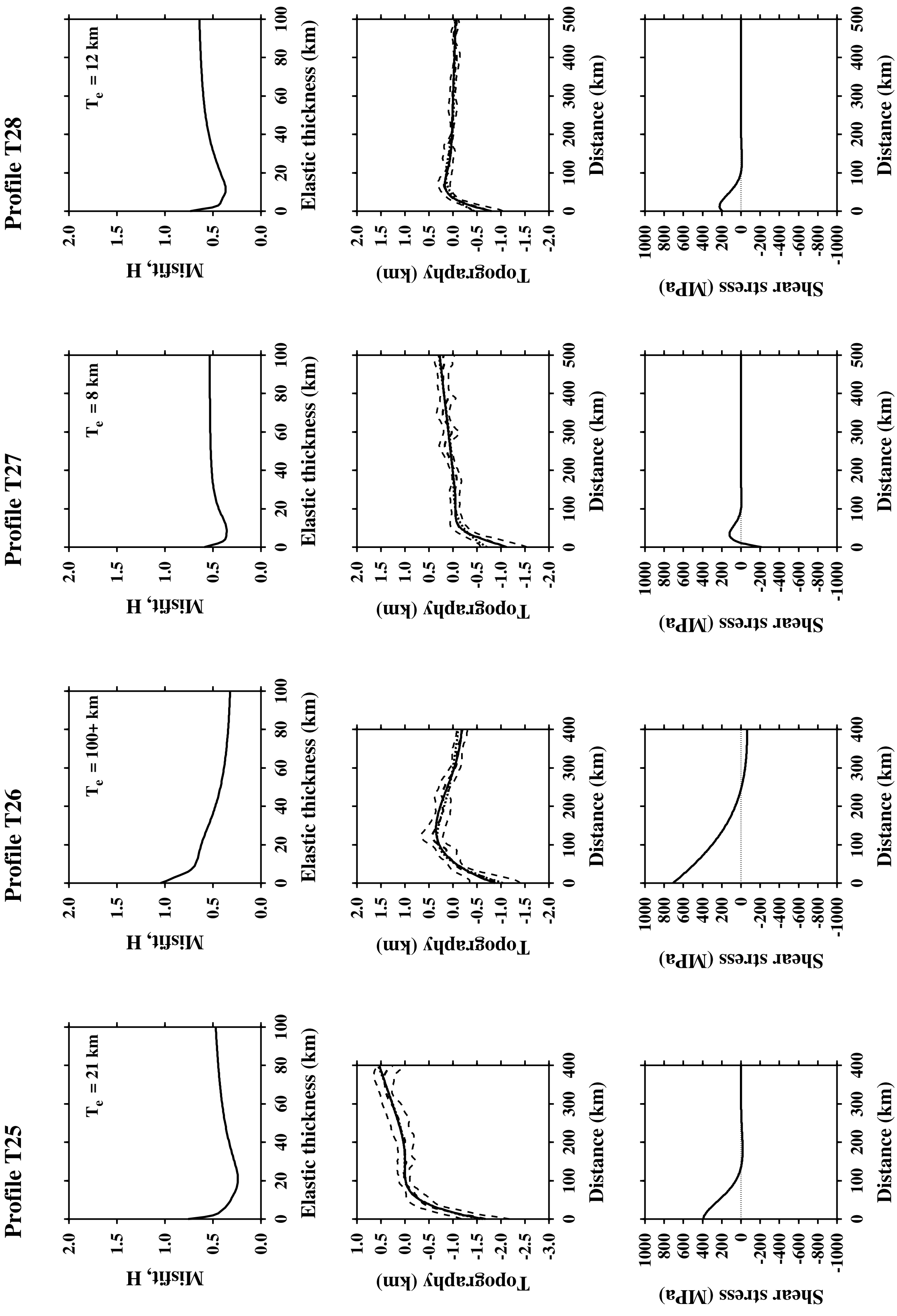

Figure A1. (continued)

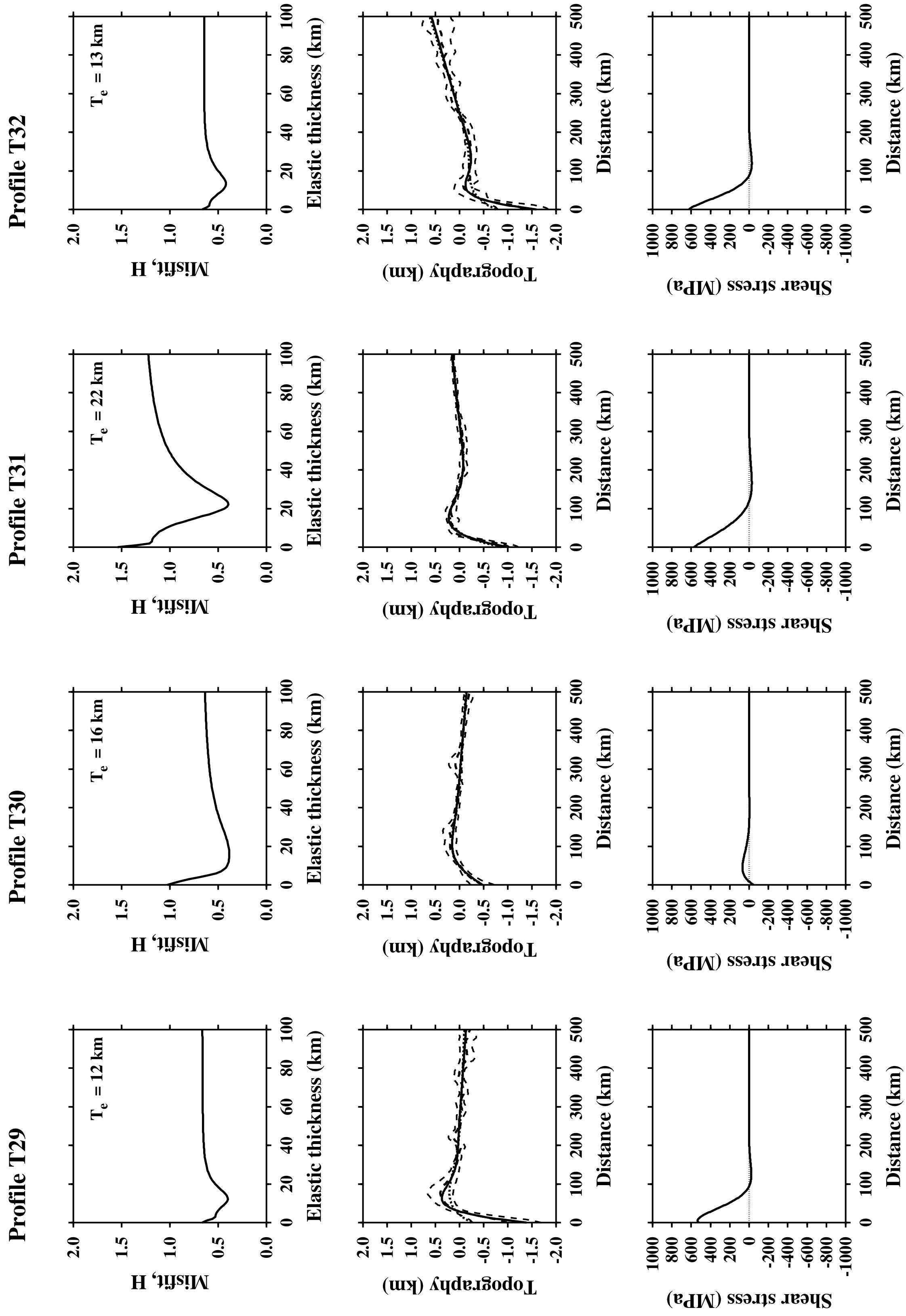

Figure A1. (continued)

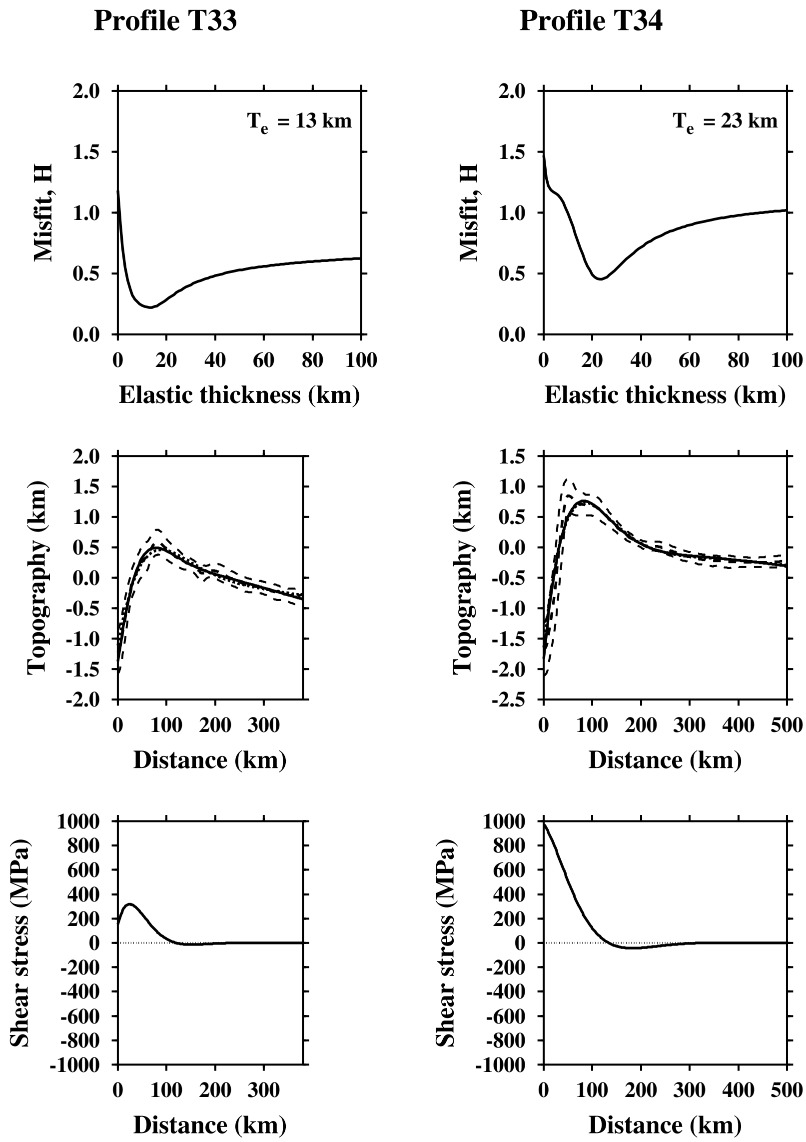

Figure A1. (continued)

modeled individually [e.g., *McKenzie and Fairhead*, 1997; *Johnson and Sandwell*, 1994] exhibit the problem that they provide good lower, but not upper, bounds on T_e.

[32] Where the observed gravity is compared with synthetic profiles calculated using the observed topography (section 3), the obtained values of T_e are generally better constrained. The gravity filter calculated using the results of an admittance study of the Beta box is generally applicable only to features within a latitude band similar to Beta. The reason for this is that most of the information in the spherical harmonic gravity field at these latitudes is derived from cycle 4, in which the altitude is approximately constant at constant latitude. If this filter is used for features at higher latitudes, the fit to the observed gravity is much poorer, and better results are achieved if a filter is produced from the results of an admittance study for a box at similarly high latitudes. However, owing to the lower resolution of the gravity field at these latitudes, the elastic thickness estimates obtained are likely to be less reliable.

[33] As with the residual topographic profiles, an elastic thickness of 25 km falls within the bounds of uncertainty, according to the misfit function, for almost all the locations at which the gravity was modeled. In the case of profiles G4 and G6, it appears that a higher T_e is necessary to produce the observed magnitude of the central gravity anomaly, given the observed topography (Figures A2a and A2b). However, the feature from which profile G6 was produced is at high latitude, and thus the T_e estimate will be poor. The topographic profile G4 is rather rough, probably mainly because the feature itself is not very axisymmetric (see Figure 5), so the estimated value of T_e in this case is also not well constrained.

[34] Considering only the best constrained estimates, produced using the gravity and topography profiles and assuming a top-loading model (section 3), the average elastic thickness is 29 ± 6 km, when the estimates are weighted according to the inverse of the squares of their uncertainties. In general, the estimates produced by modeling the residual topography using an end-loading model (section 2) tend to be smaller (giving a mean value of 22 ± 4 km), although the difference is unlikely to be significant owing to the flatness of the minima in the misfit functions. These values are also in close agreement with the average value of the T_e estimates carried out in the frequency domain (24 ± 1 km) by *Barnett et al.* [2000], who also assume top loading. There is also some tendency for T_e estimates to be slightly greater when the data quality is good, particularly when modeling is carried out in the frequency domain [see, e.g., *McKenzie and Nimmo*, 1997; *Barnett et al.*, 2000]. However, these numbers show no evidence that the values of

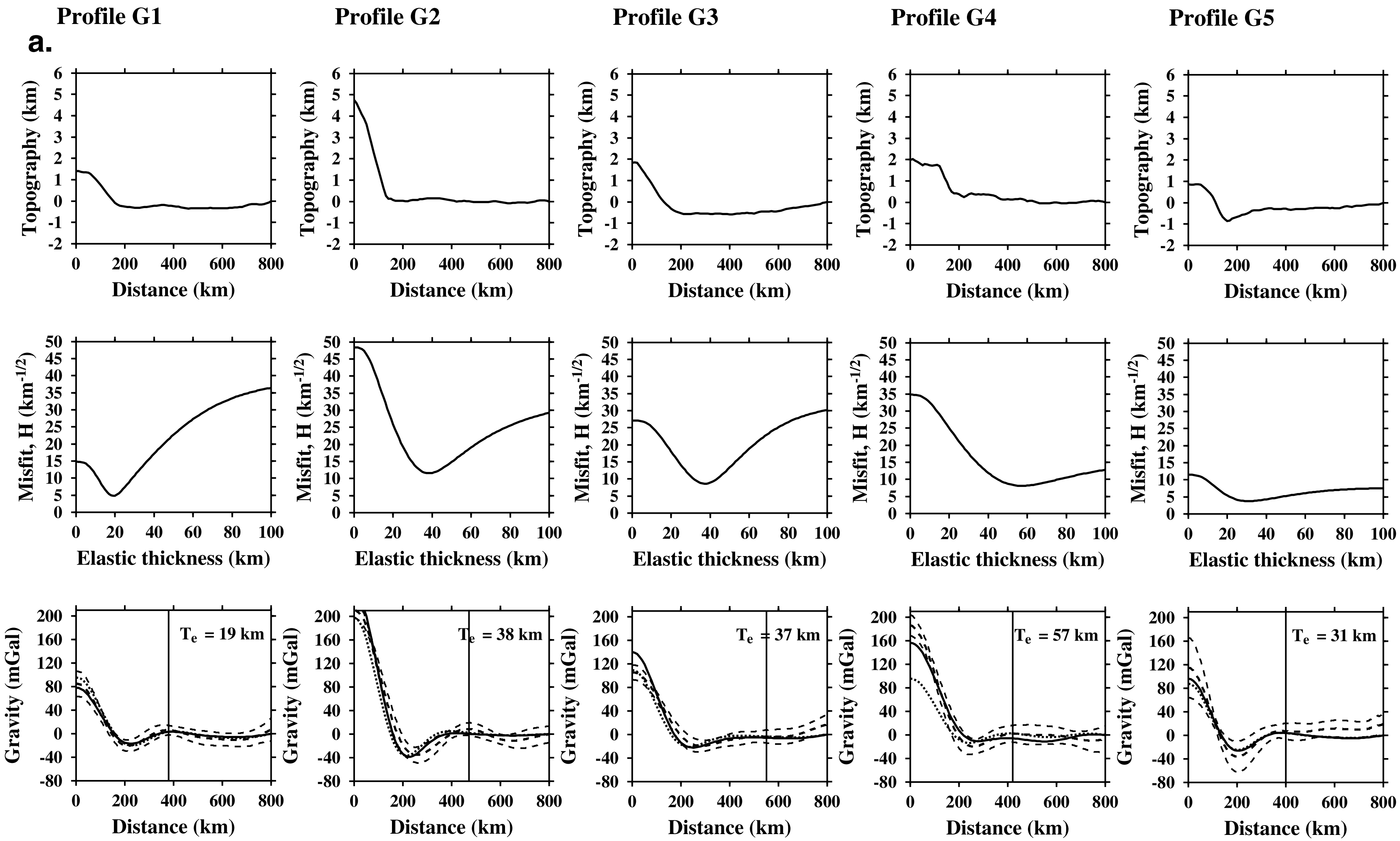

Figure A2. (a) Results for the five profiles (G1–G5) calculated from the spherical harmonic gravity, using the observed raw topography and the filter calculated using the results of an admittance study of the "Beta" box (see Figures 2–4). The top plots show the average topographic profiles as a function of radial distance. The center plots show the minimum misfit between the calculated and observed gravity profiles as a function of elastic thickness. The mimima in these curves give the best fit elastic thickness for each location, which is used to calculate the best fit gravity profile, shown in the bottom plot as a solid line. Also shown in each case is the observed gravity profile (dashed line) plus and minus the standard deviation at each point (thin dashed lines) as a function of radial distance. The value of r_o, the maximum radius out to which the misfit is calculated, is shown by a vertical line. In addition, the best fit calculated profile, assuming an elastic thickness of 25 km, in shown in each case by a dotted line. (b) The results for profiles G6 and G7 calculated from the spherical harmonic gravity, using the observed raw topography but using the filter calculated using the results of an admittance study of the "South of Ovda" box (see Figures 2, 3, and 6), shown as in Figure A2a).

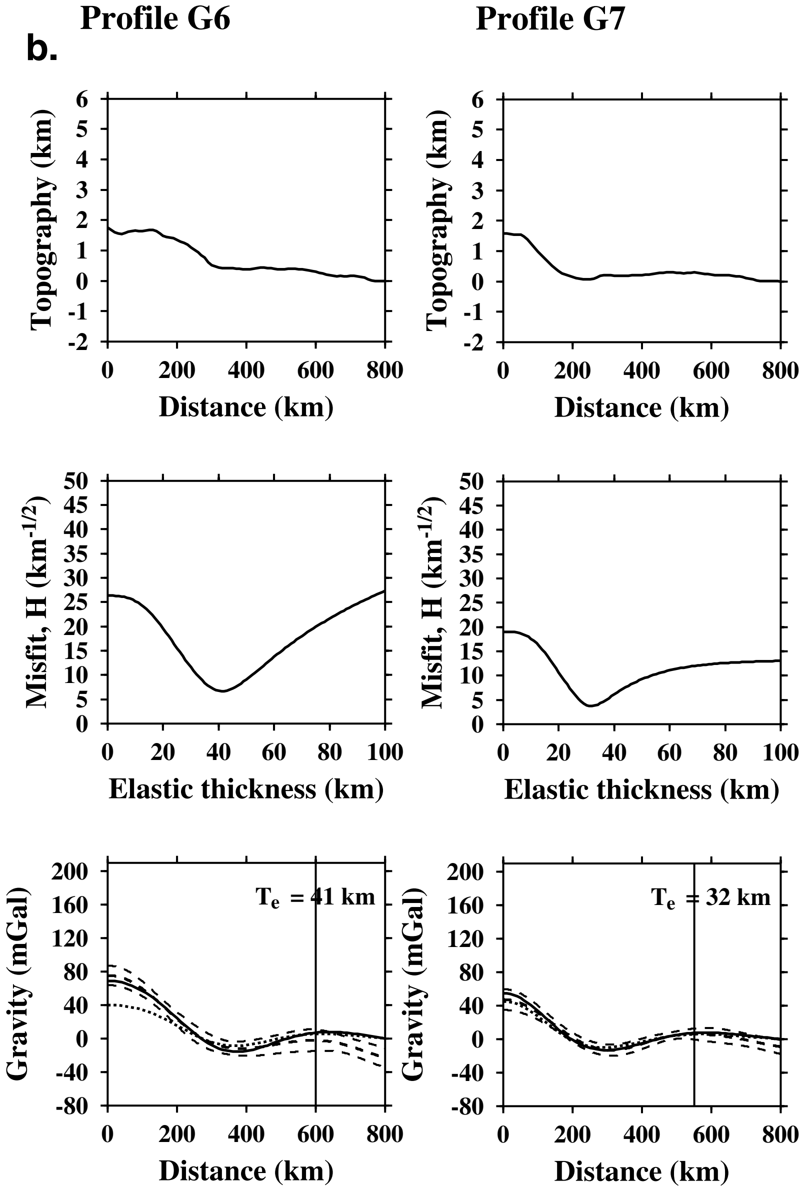

Figure A2. (continued)

$T_e$obtained using a top-loading model are smaller than those obtained assuming end loading, and overall, there is no convincing evidence that the elastic thickness of the lithosphere of Venus is anywhere outside the range of 29 ± 6 km quoted above.

[35] As discussed by *Barnett et al.* [2000], an elastic thickness for Venus which is similar to that observed in shields and old ocean basins on Earth is surprising, given that the surface temperature on Venus is so much higher (450°C). This temperature is roughly equal to that which is suspected to mark the base of the elastic layer on Earth [*Watts*, 1994]. In other words, the lithosphere of Venus must be able to support elastic stresses at higher temperatures than on Earth, which is consistent with the hypothesis that the Venusian lithosphere is dry [*Nimmo and McKenzie*, 1998].

[36] The T_e estimates obtained in this work show no clear regional variations but are noisy owing to the poor constraint on this parameter. If small-scale variations in T_e exist between different areas, within the observed range of 29 ± 6 km, these variations might become apparent if T_e is plotted against some other parameter to which it is related. One obvious possibility is age, the only currently available measure of which is crater densities. *Schaber et al.* [1998] produced a global database of the locations of the 967 impact craters identified on Venus (available at http://wwwflag.wr.usgs.gov/USGSFlag/Space/venus). From this a global map of crater density was produced by counting the craters in the vicinity of an equally spaced array of points over the surface. The crater counts were windowed by a Gaussian function, of standard deviation 1000 km, such that the craters nearest to the point in question are most heavily weighted in the counting process. Although the resulting map shows some variations in crater density between different regions, the global distribution of craters is indistinguishable from a random one [see, e.g., *Turcotte et al.*, 1999], suggesting that the surface age is globally fairly uniform [see, e.g., *Basilevsky et al.*, 1997]. Figure 7 is a plot of the elastic thickness estimates obtained in sections 2 and 3 against the dimensionless crater counts for the same locations. This plot shows no clear correlation between T_e and age.

[37] This situation is in contrast to the Earth, where regional variations in T_e are clearly resolved. Low values of elastic thickness are observed at spreading ridges, owing to the elevated thermal gradient, and in active mountain belts, which

are probably weak because of the presence of water in the crust. Conversely, high values of elastic thickness on Earth are associated with continental shields and old oceanic lithosphere, where T_e reaches approximately 35–40 km. On continents, lithospheric strength is most likely maintained by stresses in the crust, not the mantle [*Maggi et al.*, 2000], and beneath oceans by stresses in the mantle. A data set of the quality of that now available for Venus would reveal this variation in T_e. The absence of resolvable variations in elastic thickness on Venus is therefore significant. On Venus the absence of features which are similar to terrestrial spreading ridges is clear from crater counts. In addition, the lithosphere is suspected to be dry. Therefore neither of the factors which are thought to be responsible for regional variations in T_e on the Earth is present on Venus. It is also true, however, that there are no good estimates of T_e from tessera regions, because the topography is so poorly determined. The origin of this problem is that the radar signal is scattered by the rough topography such that it is difficult to pick the first return [see *McKenzie and Nimmo*, 1997, Figure 17; *Barnett et al.*, 2000]. This scattering can lead to large errors in the planetary radius [*McKenzie and Nimmo*, 1997]. On Venus we have as yet no method of dating the lithosphere; crater counts only allow dating of the surface layer, which may be relatively recently emplaced. There is therefore no way of knowing whether the deeper part of the lithosphere is much older than the surface layer. However, $T_e$estimates themselves as yet provide no evidence for the existence of variations in lithospheric properties on Venus.

Appendix A

[38] This appendix contains plots of the profiles constructed from the residual topography (as discussed in section 2.2) (Figure A1) and those constructed from the spherical harmonic gravity (section 3.2) (Figure A2).

[39] **Acknowledgments.** We would like to thank Jim Alexopoulos and Peter Ford for their assistance and Susan Smrekar and Walter Kiefer for their reviews. This work was carried out with the support of Schlumberger Cambridge Research, the Newton Trust, Magdalene College, and grants from the Royal Society and the Natural Environment Research Council. Department of Earth Sciences, Cambridge University, contribution 6506.

References

Barnett, D. N., F. Nimmo, and D. McKenzie, Elastic thickness estimates for Venus using line of sight accelerations from Magellan cycle 5, *Icarus*, *146*, 404–419, 2000.

Basilevsky, A. T., J. W. Head, G. G. Schaber, and R. G. Strom, The resurfacing history of Venus, in *Venus II*, edited by S. W. Bougher, D. M. Hunten and R. J. Phillips, pp. 1047–1084, Univ. of Ariz. Press, Tucson, 1997.

Brown, C. D., and R. E. Grimm, Lithospheric rheology and flexure at Artemis Chasma, Venus, *J. Geophys. Res.*, *101*, 12,697–12,708, 1996a.

Brown, C. D., and R. E. Grimm, Floor subsidence and rebound of large Venus craters, *J. Geophys. Res.*, *101*, 26,057–26,067, 1996b.

Foster, A., and F. Nimmo, Comparisons between the rift systems of East Africa, Earth and Beta Regio, Venus, *Earth Planet. Sci. Lett.*, *143*, 183–195, 1996.

Grimm, R. E., and P. C. HessThe crust of Venus, in *Venus II*, edited by S. W. Bougher, D. M. Hunten, and R. J. Phillips, pp. 1205–1244, Univ. of Ariz. Press, Tucson, 1997.

Johnson, C. L., and D. T. Sandwell, Lithospheric flexure on Venus, *Geophys. J. Int.*, *119*, 627–647, 1994.

Kaula, W. M., *Theory of Satellite Geodesy*, Blaisdell, Waltham, Mass., 1966.

Kiefer, W. S., and E.-K. Potter, Gravity anomalies at Venus shield volcanoes: Implications for lithospheric thickness, *Lunar Planet. Sci.*, *XXXI*, abstract 1924, 2000.

Konopliv, A. S., W. B. Banerdt, and W. L. Sjogren, Venus gravity: 180th degree and order model, *Icarus*, *139*, 3–18, 1999.

Maggi, A., J. A. Jackson, D. McKenzie, and K. Priestley, Earthquake focal depths, effective elastic thickness, and the strength of the continental lithosphere, *Geology*, *28*, 495–498, 2000.

McGovern, P. J., and S. C. Solomon, Growth of large volcanoes on Venus: Mechanical models and implications for structural evolution, *J. Geophys. Res.*, *103*, 11,071–11,101, 1998.

McKenzie, D., The relationship between topography and gravity on Earth and Venus, *Icarus*, *112*, 55–88, 1994.

McKenzie, D., and D. Fairhead, Estimates of the effective elastic thickness of the continental lithosphere from Bouguer and free air gravity anomalies, *J. Geophys. Res.*, *102*, 27,523–27,552, 1997.

McKenzie, D., and F. Nimmo, Elastic thickness estimates for Venus from line of sight accelerations, *Icarus*, *130*, 198–216, 1997.

Nimmo, F., and D. McKenzie, Volcanism and tectonics on Venus, *Annu. Rev. Earth Planet. Sci.*, *26*, 23–51, 1998.

Phillips, R. J., Estimating lithospheric properties at Atla Regio, Venus, *Icarus*, *112*, 147–170, 1994.

Phillips, R. J., C. L. Johnson, S. J. Mackwell, P. Morgan, D. T. Sandwell, and M. T. Zuber, Lithospheric mechanics and dynamics of Venus, in *Venus II*, edited by S. W. Bougher, D. M. Hunten, and R. J. Phillips, pp. 1163–1204, Univ. of Ariz. Press, Tucson, 1997.

Rappaport, N. J., A. S. Konopliv, and A. B. Kucinskas, An improved 360 degree and order model of Venus topography, *Icarus*, *139*, 19–31, 1999.

Rogers, P. G., and M. T. Zuber, Tectonic evolution of Bell Regio, Venus: Regional stress, lithospheric flexure and edifice stresses, *J. Geophys. Res.*, *103*, 16,841–16,853, 1998.

Sandwell, D. T., and G. Schubert, Flexural ridges, trenches and outer rises around coronae on Venus, *J. Geophys. Res.*, *97*, 16,069–16,083, 1992.

Schaber, G. G., R. L. Kirk, and R. G. Strom, Data base of impact craters on Venus based on analysis of Magellan radar images and altimetry data, *U.S. Geol. Surv. Open File Rep.*, 98–104, 1998.

Simons, M., S. C. Solomon, and B. H. Hager, Localization of gravity and topography: Constraints on the tectonics and mantle dynamics of Venus, *Geophys. J. Int.*, *131*, 24–44, 1997.

Smrekar, S. E., Evidence for active hotspots on Venus from analysis of Magellan gravity data, *Icarus*, *112*, 2–26, 1994.

Smrekar, S. E., and E. R. Stofan, Origin of corona-dominated topographic rises on Venus, *Icarus*, *139*, 100–115, 1999.

Smrekar, S. E., W. S. Kiefer, and E. R. Stofan, Large volcanic rises on Venus, in *Venus II*, edited by S. W. Bougher, D. M. Hunten, and R. J. Phillips, pp. 845–878, Univ. of Ariz. Press, Tucson, 1997.

Snyder, J. P., An album of map projections, *U.S. Geol. Surv. Prof. Pap.*, 1453, 1989.

Solomon, S. C., and J. W. Head, Lithospheric flexure beneath the Freyja Montes foredeep, Venus: Constraints on lithospheric thermal gradient and heat flow, *Geophys. Res. Lett.*, *17*, 1393–1396, 1990.

Tiwari, V. M., and D. C. Mishra, Estimation of effective elastic thickness from gravity and topography data under the Deccan Volcanic Province, India, *Earth Planet. Sci. Lett.*, *171*, 289–299, 1999.

Turcotte, D. L., G. Morein, D. Roberts, and B. D. Malamud, Catastrophic resurfacing and episodic subduction on Venus, *Icarus*, *139*, 49–54, 1999.

Watts, A. B., Crustal structure, gravity anomalies and flexure of the lithosphere in the vicinity of the Canary Islands, *Geophys. J. Int.*, *119*, 648–666, 1994.

Watts, A. B., J. H. Bodine, and N. M. Ribe, Observations of flexure and the geological evolution of the Pacific Ocean basin, *Nature*, *283*, 532–537, 1980.

D. N. Barnett, D. McKenzie, and F. Nimmo, Bullard Laboratories, Department of Earth Sciences, University of Cambridge, Madingley Road, Cambridge, CB3 0EZ, England UK. (barnett@esc.cam.ac.uk)

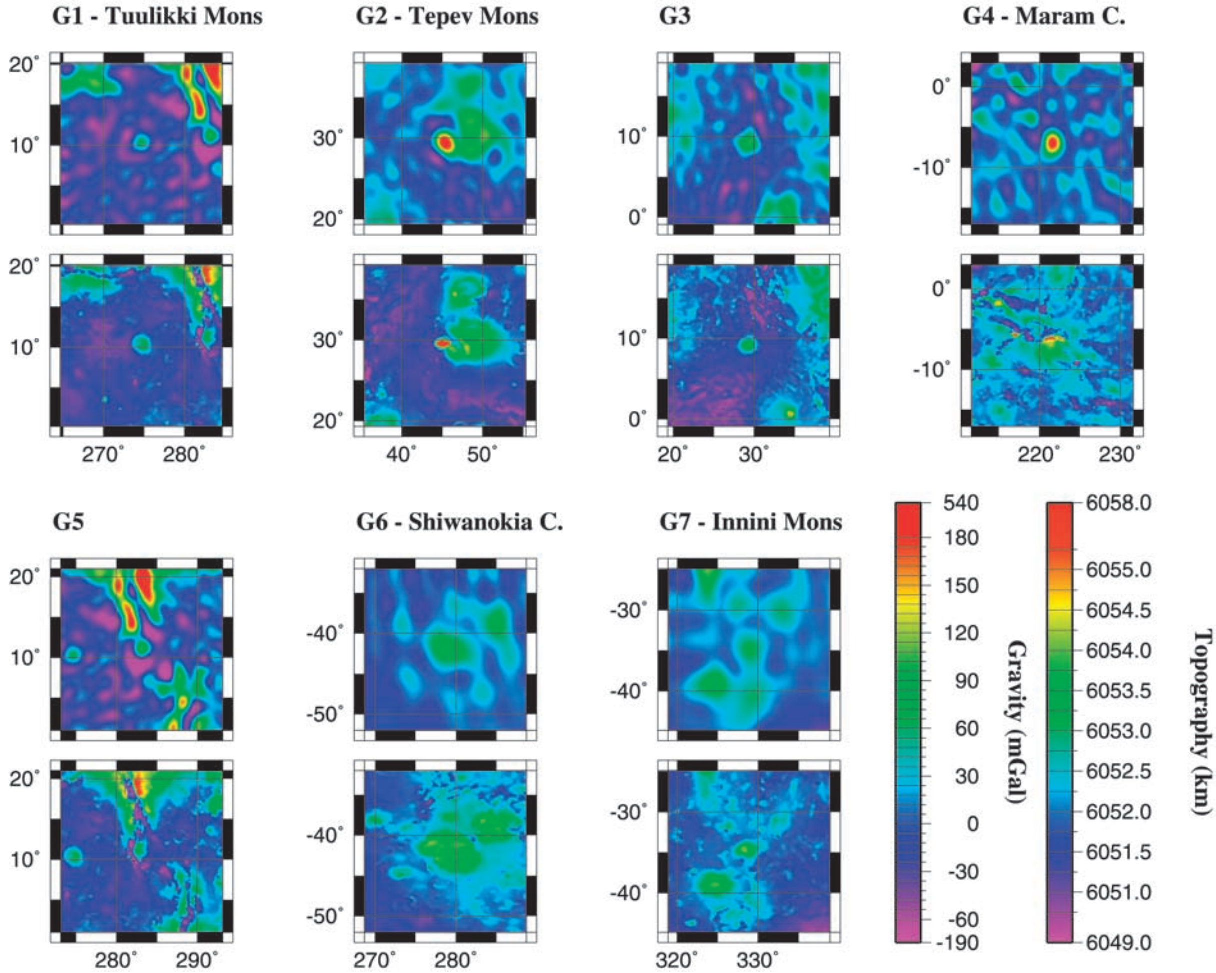

Figure 5. Venus gravity in mGal, calculated from the spherical harmonic model to $l = m = 180$ [*Konopliv et al.*, 1999] (top plots) and raw topography (bottom plots), for the locations of the seven features (center of each box) from which radial profiles were calculated and the elastic thickness was estimated.